RESEARCH ARTICLE | JULY 25 2024

Graded metamaterial with broadband active controllability for low-frequency vibration suppression
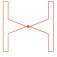
Yupei Jian ⓘ ; Guobiao Hu ⓘ ; Lihua Tang ✉ ⓘ ; Jiawen Xu ⓘ ; Deqing Huang ⓘ ; Kean Aw ⓘ

Check for updates
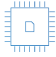
View Online   Export Citation

Graded metamaterial with broadband active controllability for low-frequency vibration suppression

Yupei Jian,[1,2] ⓘ Guobiao Hu,[3] ⓘ Lihua Tang,[2,a)] ⓘ Jiawen Xu,[4] ⓘ Deqing Huang,[1] ⓘ and Kean Aw[2] ⓘ

AFFILIATIONS

[1]School of Electrical Engineering, Southwest Jiaotong University, Chengdu, Sichuan 610031, China
[2]Department of Mechanical and Mechatronics Engineering, The University of Auckland, Auckland 1010, New Zealand
[3]Internet of Things Thrust, The Hong Kong University of Science and Technology (Guangzhou), Guangzhou, Guangdong 511400, China
[4]School of Instrument Science and Engineering, Southeast University, Nanjing, Jiangsu 210096, China

[a)]Author to whom correspondence should be addressed: l.tang@auckland.ac.nz

ABSTRACT

This paper presents a new class of graded metamaterial beams by leveraging actively controllable resonators (ACR). The metamaterial comprises a homogeneous host beam that is mounted with negative capacitance shunted piezoelectric cantilever beams, each of which has a tip mass block. Properly changing the negative capacitances (NCs) in the stiffening/softening shunt circuits can control the formed bandgaps, providing greater adjustability and flexibility. Specifically, using modal analysis and considering higher modes of flexural vibrations, the ACR is simplified to an equivalent lumped parameter system with a correction factor applied to the reaction force. We demonstrate the relationship between the derived equivalent parameters of the ACR and NC for different circuitry configurations. A finite element model is built to validate the theoretical models of the ACR and the proposed metamaterial. Subsequently, a grading strategy is proposed to determine the NC values of ACR arrays for achieving broadband vibration suppression. A mechanical damping enhancement phenomenon that can contribute to forming an aggregated band is observed when resistances are introduced into the stiffening circuits. Three circuit configurations are examined, i.e., stiffening, softening, and hybrid circuits. The results showed that a proper grading coefficient can effectively suppress broadband vibration in the low-frequency range.

I. INTRODUCTION

The growing demand for energy efficiency and space optimization in advanced engineering has increased the popularity of lightweight and high-strength materials/structures. This trend is particularly evident in the fields of aerospace,[1] automobiles,[2] and civil engineering,[3,4] where the use of lightweight materials with high stiffness has become prevalent. Traditional methods, such as vibration absorbers[5] and viscoelastic materials,[6] face significant difficulties in effectively suppressing low-frequency vibrations for lightweight structures. In recent decades, locally resonant metamaterials have emerged as a promising approach for mitigating low-frequency vibrations. Characterized by their periodic structures incorporating local resonators, locally resonant metamaterials can suppress sub-wavelength waves by opening locally resonant bandgaps. Low-frequency vibration suppression can be realized without constraints on the lattice constant,[7,8] which is an extraordinary advantage over Bragg scattering-based phononic crystals,[9] and shows great application prospects for structural vibration suppression of large aircraft, rockets, and ships.[10,11] For the sake of brevity, the term "metamaterial" is used hereafter for locally resonant metamaterials.

In this domain, considerable focus has been placed on active metamaterials. Researchers refer to a metamaterial with components that can be reconfigured in service as an active metamaterial.[12,13] The term "active" emphasizes the tunability and reconfigurability of metamaterials. Generally, by introducing

reconfigurable components into a metamaterial system, the bandgap can be actively tuned without necessitating physical alterations to the microstructures, making them suitable for various vibrational environments. One way to realize it is to integrate smart materials, such as piezoelectric materials,[14,15] magnetorheological elastomers,[16,17] and shape memory alloys,[18,19] into the microstructures of metamaterials, thereby enabling the tuning of bandgaps through the control of these smart materials. Among these, active metamaterials based on piezoelectric shunt technology have garnered considerable interest due to their ultra-light additional mass and wide frequency adjustment range.[20,21] By modifying the shunt circuit, the center frequency of the bandgap can be easily adjusted from a few tens of hertz to a few kilohertz. However, the bandwidth of the bandgap when the shunt circuit is fixed is narrow due to the relatively weak electromechanical coupling between piezoelectric materials and the underlying structure.[22] In some applications, such as vibration suppression of aerospace structures subjected to aerodynamic loads[23] or offshore structures with ocean environmental loads,[24] a narrower bandgap is not attractive due to the broadband nature of the external excitation. To this end, various advanced shunt circuits have been proposed to enhance the bandgap strength and width, including negative capacitance (NC) circuits,[25–27] nonlinear electrical networks using synchronized switching damping on inductors,[28,29] and nonlinear capacitor circuits.[30] In addition to improving the shunt circuits, other researchers worked on optimizing the configuration of the unit lattice of metamaterials to widen the bandgap. Graded metamaterials, i.e., a quasi-periodic metamaterial achieved by gradually varying the configuration of the unit cell, showed potential in enlarging the bandgap.[31,32] Many researchers considered gradually modifying the geometric/material properties of the local resonators, including the stiffness/mass of mass-spring resonators,[33,34] the height of Helmholtz resonators,[35] and the length of beam-type resonators,[36] to broaden the vibration suppression region of metamaterials. However, it must be mentioned that once these metamaterials are fabricated, it is difficult to modify their grading configuration. To deal with this limitation, active metamaterials based on piezoelectric shunt technology, which make them ideal for designing graded metamaterials, are used. Alshaqaq and Erturk[37] designed a graded metamaterial by attaching piezoelectric arrays connected to different impedances obtained in accordance with a grading strategy to a host structure. Uniformly distributed discrete bandgaps were generated, forming a wide vibration attenuation region. With the same concept, Liu *et al.*[38] replaced the resistive-inductive circuit in Ref. 37 with an NC circuit. It is found that the NC circuit enhanced the electromechanical coupling. A wide attenuation zone was observed in the high-frequency region spanning over 7000–11 000 Hz. Recent studies[39,40] have further extended this concept by proposing a disordered design for impedance values in the shunts by using optimization techniques, which lead to optimal vibration attenuation performance. In our previous work,[41] we analytically and experimentally showcased the broadening effect of the bandgap in a graded piezoelectric metamaterial induced by geometric variations. Overall, the aforementioned works achieved broadband vibration control in the medium-high-frequency range by directly affixing the shunted piezoelectric cell to the substrate/host structure. However, our previous experiment[41] showed that when the

bandgap is tuned to low-medium frequencies (below 300 Hz), the bandgap becomes narrow and weak, and non-uniform designs have limited efficacy in widening the low-frequency bandgap.

The focus of this work is on achieving active control of metamaterials for broadband vibration suppression in low-frequency regions. To this end, a graded metamaterial with actively controllable resonators (ACRs) is designed. The resonator array comprises piezoelectric cantilever beams shunted to varying NCs. Compared to conventional configurations, the vibration suppression strength of the bandgap generated by out-of-phase motions of beam-type resonators is expected to be significantly stronger. It is known that when a piezoelectric material is shunted to an NC circuit, its elastic modulus can be controlled by varying the NC circuit.[42–44] Based on this concept, Chen *et al.*[45] conceptualized a metamaterial with controllable resonators to actively tune the bandgap. However, only a qualitative analysis of the effect of the NC circuit on bandgap tuning has been carried out. Achieving graded metamaterials using ACRs for broadband low-frequency vibration control faces several challenges:

(1) Implementing the effective grading pattern for tuning the NC circuits requires an accurate model of the ACR, which has not yet been developed.
(2) It is unclear how NC affects the equivalent parameters of an ACR, which is a composite structure containing NC-shunted piezoelectric elements.
(3) Different NC values typically have stiffening/softening effects on piezoelectric components. The difference between employing ACRs with stiffening or softening effects in the construction of graded metamaterials is unknown.

This paper addresses the above issues and is structured as follows. Section II provides an overview of the graded metamaterial with ACR. The theoretical models of the ACR and the graded metamaterial after assembling ACRs to the host beam are established. Section III analyzes the effect of the NC circuit on the equivalent parameters of the ACR, based on which a graded strategy for adjusting the NC circuits is proposed. Model validation using the finite element (FE) method is reported in Sec. IV. Section V demonstrates the broadband vibration suppression performance of the proposed metamaterial in the low-frequency region. Conclusive remarks are presented in Sec. VI.

II. THEORETICAL MODELING

Figure 1(a) shows the schematic of a graded metamaterial system comprising a host beam equipped with $2s + 1$ beam-type actively controllable resonators (ACRs) arranged periodically. A locally resonant bandgap is formed when subjected to flexural waves, as the parasitic beams generate "cancellation" reaction forces at the roots due to out-of-plane motions. To counter the undesired torsional motions, ACRs are mounted in pairs on both sides in symmetry to maintain force balance. A closer view of the ACR is presented in Fig. 1(b), which shows a small cantilever beam. Two piezoelectric patches of lead zirconate titanate (PZT) with identical pole directions partially cover the top and bottom of the cantilever beam from the root. To reduce the fundamental natural frequency of ACRs, a homogeneous mass block M_t is attached to the tip end.
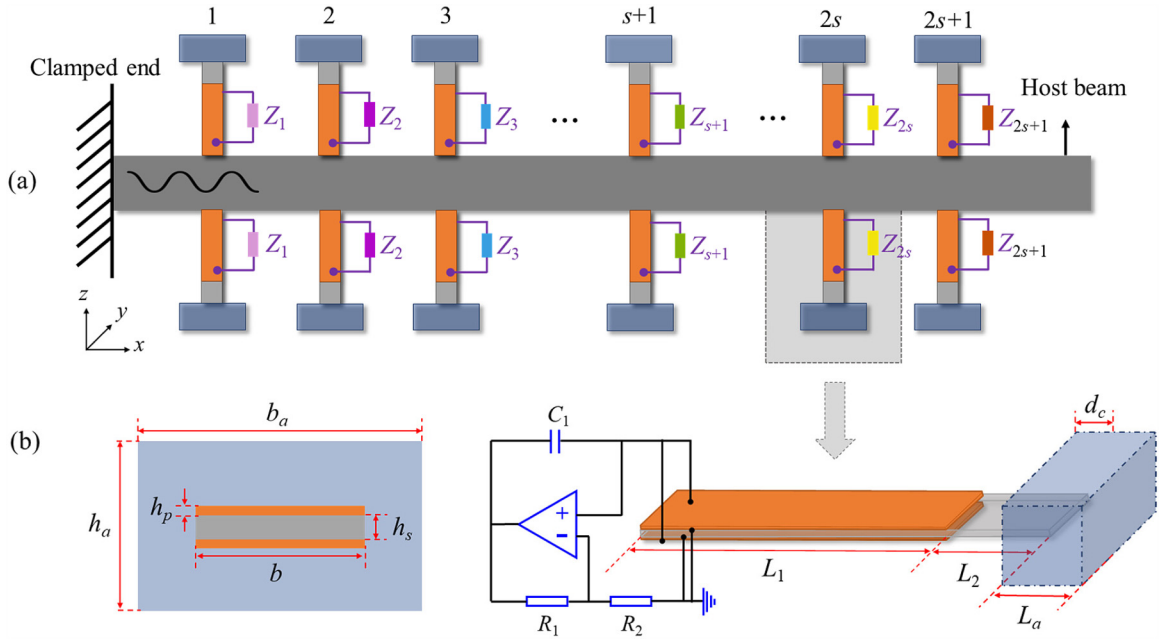
03 August 2024 11:14:43

FIG. 1. (a) Schematic of a graded metamaterial system attached with ACRs; (b) an enlarged view of the ACR, where NC is represented by an OP-AMP-based analog circuit.

An NC with impedance $Z = 1/(i\omega C_N)$ is shunted to the PZT patches. The NC shunting techniques can increase or decrease the elastic modulus of the shunted PZT and have been applied in a variety of fields. For instance, Kuchibhatla and Leamy[46] integrated NC circuits onto valley-Hall topological insulators to achieve reconfigurable interface states. In our work, NC can actively change the physical properties of the ACR, allowing the ACR to be treated as an electromechanical resonator. Since the impedance of an actual capacitor cannot be negative, a common implementation of NC is chosen here, i.e., an analog circuit based on operational amplifiers (OP-AMPs),[27] to represent the NC, as shown in Fig. 1(b). Note that the OP-AMP in Fig. 1(b) is considered ideal so that the desired NC value $C_N = -R_1 C_1/R_2$ can be obtained. Issues arising from the practical OP-AMP will be discussed in Sec. III B. In this work, the NC shunted to each ACR varies based on a grading design strategy, which will be elaborated in Sec. III C. The impedances assigned to different ACRs are denoted by Z_j, $j = 1$, $2, \ldots, s + 1, \ldots, 2s + 1$, as shown in Fig. 1(a).

A. Equivalent lumped model of an actively controllable resonator

The ACR shown in Fig. 1(b) can be modeled as a SDOF (Single Degree of Freedom) system with equivalent stiffness k and mass m based on Hooke's law,[47,48]

$$m = \frac{33}{140} M_c + M_t, \quad k = \frac{3EI_{\text{eff}}}{L_s^3}, \tag{1}$$

where M_c and EI_{eff} are the mass and effective bending stiffness of the composite beam, respectively. $L_s = L_1 + L_2$ is the length of the substrate of the ACR. In real-life applications, the length of the ACR is limited due to two factors: (1) The piezoelectric patch should cover a large substrate area to change the overall modulus effectively; and (2) Excessively long piezoelectric patches are prone to break. Consequently, Eq. (1) incurs significant errors for relatively short beams, as the mass block dimensions are not negligible compared to the cantilever beam length and, thus, can no longer be regarded as a point mass. Since even a minor adjustment to the negative capacitance value leads to a substantial change in the equivalent parameters of the ACR, the accuracy of the simplified model based on Eq. (1) is insufficient. Achieving precise tuning of the ACR is challenging in this context. Thus, this paper commences with developing a refined lumped system model for the ACR using modal analysis.

The governing equation of the jth ACR can be expressed as

$$\begin{cases} EI_{a,1} \dfrac{\partial^4 w_a(x_1, t)}{\partial x_1^4} + m_{a,1} \dfrac{\partial^2 w_a(x_1, t)}{\partial t^2} = -m_{a,1} \ddot{w}(\tilde{x}_j, t), \\ EI_{a,2} \dfrac{\partial^4 w_a(x_2, t)}{\partial x_2^4} + m_{a,2} \dfrac{\partial^2 w_a(x_2, t)}{\partial t^2} = -[m_{a,2} + M_t \delta(x_2 - L_2)] \ddot{w}(\tilde{x}_j, t), \end{cases} \tag{2}$$

where $w_a(x, t)$ and $w(\tilde{x}_j, t)$, respectively, denote the relative beam deflection of the ACR and the base motion, in which x_1 and x_2 are the local coordinates of beam sections with and without PZT coverage, respectively (i.e., $0 \leq x_1 \leq L_1$, $0 \leq x_2 \leq L_2$). $\tilde{x}$ is the coordinate

of the host beam, and the base motion $w(\tilde{x}_j, t)$ refers to the absolute displacement of the host beam where the jth ACR is mounted. $EI_{a,n}$ and $m_{a,n}$, $n = 1, 2$, respectively, denote the effective bending stiffness and mass per length of the beam sections 1 and 2 of the ACR). M_t is the tip mass. d_c is the distance from the mass block's center of gravity to the beam's attachment point. Since the mass block is homogeneous, we have $d_c = L_a/2$, as shown in Fig. 1(b). The relevant material parameters in Eq. (2) have been labeled in Fig. 2.

The equivalent parameters can be obtained as

$$\begin{cases} EI_{a,1} = E_s \dfrac{bh_s^3}{12} + E_p(\omega)\left[\dfrac{2b}{3}\left(\left(h_p + \dfrac{h_s}{2}\right)^3 - \dfrac{h_s^3}{8}\right)\right], \\ EI_{a,2} = E_s \dfrac{bh_s^3}{12}, \\ m_{a,1} = b(\rho_s h_s + 2\rho_p h_p), \\ m_{a,2} = b\rho_s h_s, \end{cases} \quad (3)$$

where E_s and $E_p(\omega)$ stand for Young's modulus of the cantilever beam and the PZT patch. ρ_s and ρ_p are the mass density of the beam and the piezoelectric patch. Flexural wave propagation in this composite beam is considered under the assumption of plane stress, whereby the effects of shear deformation and rotary inertia of the beam's cross section are neglected, leading to the 1D constitutive relation for the PZT patch,[49]

$$\begin{bmatrix} D_3 \\ S_1 \end{bmatrix}\begin{bmatrix} \varepsilon_{33}^T & d_{31} \\ d_{31} & s_{11}^E \end{bmatrix} = \begin{bmatrix} E_3 \\ T_1 \end{bmatrix}, \quad (4)$$

where D_3 and E_3 represent the electrical displacement and the electric field along the z-direction, respectively. S_1 and T_1 are the strain and stress along the x-direction. ε_{33}^T is the dielectric constant at constant strain. d_{31} is the piezoelectric strain constant. s_{11}^E is the compliance coefficient at a constant electric field. When shunted to an external impedance Z, the modulus of the PZT becomes[50]

$$E_p(\omega) = E_p^{\text{oc}}\left(1 - \frac{k_{31}^2}{1 + i\omega C_p^S Z}\right), \quad (5)$$

where $E_p^{\text{oc}} = E_p^{\text{sc}}/(1 - k_{31}^2)$ is Young's modulus of the PZT patch under the open-circuit condition, in which $E_p^{\text{sc}} = 1/s_{11}^E$ is Young's modulus under the short-circuit condition. k_{31} is the electromechanical coupling coefficient. $C_p^S = (2\varepsilon_{33}^S bL_1)/h_p$ is the internal
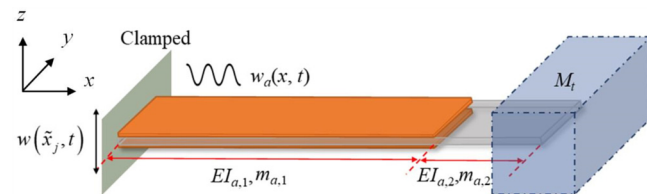
capacitance of the PZT patch at constant strain. To facilitate the analysis, a negative capacitance ratio (NCR) $\lambda = -C_N/C_p^S$ is defined, and Eq. (5) can be rewritten as

$$E_p(\omega) = E_p^{\text{oc}}\left(1 - \frac{k_{31}^2}{1 - 1/\lambda}\right). \quad (6)$$

To simplify the ACR as a lumped system, its mode shape and the natural frequency are first derived. Using the variation-separation method, the deflection of the composite beam relative to the host beam can be expressed as

$$w_{a,n}(x_n, t) = \phi_n(x_n)\eta(t), \quad (7)$$

where $\phi_n(x_n)$ is the mode shape of beam section n. $\eta(t)$ is the modal coordinate. We first consider the free vibration of the ACR and omit the force term on the right-hand side of Eq. (2). Substituting Eq. (7) into the governing equation of free vibration and neglecting $\eta(t)$, one can obtain

$$EI_{a,n}\frac{d^4\phi_n(x_n)}{dx_n^4} - \omega^2 m_{a,n}\phi_n(x_n) = 0. \quad (8)$$

The general solution of Eq. (8) can be expressed as

$$\phi_n(x_n) = A_n \sin\beta_n x_n + B_n \cos\beta_n x_n + C_n \sinh\beta_n x_n + D_n \cosh\beta_n x_n, \quad (9)$$

where $\beta_n^4 = (\omega^2 m_{a,n})/(EI_{a,n})$. Considering the boundary conditions of displacement, rotation angle, bending moment, and shear force at the clamped end, tip end, and the interface between beam sections 1 and 2, one can obtain

$$\begin{cases} \phi_1(0) = 0, \\ \phi_1'(0) = 0, \\ \phi_1(L_1) = \phi_2(0), \\ \phi_1'(L_1) = \phi_2'(0), \end{cases} \begin{cases} EI_{a,1}\phi_1''(L_1) = EI_{a,2}\phi_2''(0), \\ EI_{a,1}\phi_1'''(L_1) = EI_{a,2}\phi_2'''(0), \\ EI_{a,2}\phi_2''(L_2) = J_t\omega^2\phi_2'(L_2) + M_t d_c\omega^2\phi_2(L_2), \\ EI_{a,2}\phi_2'''(L_2) = -M_t d_c\omega^2\phi_2'(L_2) - M_t\omega^2\phi_2(L_2), \end{cases} \quad (10)$$

where J_t is the moment of inertia of the mass block about the axis that passes through the attachment point. Substituting Eq. (9) into Eq. (10), rewriting it into the matrix form, and forcing the determinant of the coefficient matrix to be zero, we have

$$\begin{vmatrix} (T_1 N_1 + T_2 N_3 + T_3 N_5 + T_4 N_7) & (T_1 N_2 + T_2 N_4 + T_3 N_6 + T_4 N_8) \\ (T_5 N_1 + T_6 N_3 + T_7 N_5 + T_8 N_7) & (T_5 N_2 + T_6 N_4 + T_7 N_6 + T_8 N_8) \end{vmatrix} = 0, \quad (11)$$

FIG. 2. Schematic of the ACR.

where

$$
\begin{cases}
Y_1 = \dfrac{\beta_1}{\beta_2} \\[4pt]
Y_2 = \dfrac{EI_{a,1}\beta_1^2}{EI_{a,2}\beta_2^2} \\[4pt]
Y_3 = \dfrac{EI_{a,1}\beta_1^3}{EI_{a,2}\beta_2^3}
\end{cases}
\begin{cases}
N_1 = [(Y_1+Y_3)\cos\beta_1 L_1 - (Y_1-Y_3)\cosh\beta_1 L_1]/2, \\
N_2 = -[(Y_3+Y_1)\sin\beta_1 L_1 + (Y_3-Y_1)\sinh\beta_1 L_1]/2, \\
N_3 = [(1+Y_2)\sin\beta_1 L_1 - (1-Y_2)\sinh\beta_1 L_1]/2, \\
N_4 = [(1+Y_2)\cos\beta_1 L_1 - (1-Y_2)\cosh\beta_1 L_1]/2, \\
N_5 = [(Y_1-Y_3)\cos\beta_1 L_1 - (Y_1+Y_3)\cosh\beta_1 L_1]/2, \\
N_6 = [(Y_3-Y_1)\sin\beta_1 L_1 - (Y_3+Y_1)\sinh\beta_1 L_1]/2, \\
N_7 = [(1-Y_2)\sin\beta_1 L_1 - (1+Y_2)\sinh\beta_1 L_1]/2, \\
N_8 = [(1-Y_2)\cos\beta_1 L_1 - (1+Y_2)\cosh\beta_1 L_1]/2,
\end{cases}
\tag{12}
$$

and

$$
\begin{cases}
T_1 = \left[-\left(EI_{a,1}\beta_2^2 + M_t d_c\omega^2\right)\sin\beta_2 L_2 - \left(M_t d_c^2 + J_t\right)\omega^2\beta_2\cos\beta_2 L_2\right], \\
T_2 = \left[-\left(EI_{a,2}\beta_2^2 + M_t d_c\omega^2\right)\cos\beta_2 L_2 + \left(M_t d_c^2 + J_t\right)\omega^2\beta_2\sin\beta_2 L_2\right], \\
T_3 = \left[\left(EI_{a,2}\beta_2^2 - M_t d_c\omega^2\right)\sinh\beta_2 L_2 - \left(M_t d_c^2 + J_t\right)\omega^2\beta_2\cosh\beta_2 L_2\right], \\
T_4 = \left[\left(EI_{a,2}\beta_2^2 - M_t d_c\omega^2\right)\cosh\beta_2 L_2 - \left(M_t d_c^2 + J_t\right)\omega^2\beta_2\sinh\beta_2 L_2\right], \\
T_5 = \left[\left(-EI_{a,2}\beta_2^3 + M_t d_c\omega^2\beta_2\right)\cos\beta_2 L_2 + M_t\omega^2\beta_2\sin\beta_2 L_2\right], \\
T_6 = \left[\left(EI_{a,2}\beta_2^3 - M_t d_c\omega^2\beta_2\right)\sin\beta_2 L_2 + M_t\omega^2\cos\beta_2 L_2\right], \\
T_7 = \left[\left(EI_{a,2}\beta_2^3 + M_t d_c\omega^2\beta_2\right)\cosh\beta_2 L_2 + M_t\omega^2\sinh\beta_2 L_2\right], \\
T_8 = \left[\left(EI_{a,2}\beta_2^3 + M_t d_c\omega^2\beta_2\right)\sinh\beta_2 L_2 + M_t\omega^2\cosh\beta_2 L_2\right].
\end{cases}
\tag{13}
$$

The kth natural frequency Ω_k of the ACR can be acquired by solving Eq. (11) to seek the non-trivial solution. Then, substituting Ω_k back into Eq. (10) to seek the solutions of the coefficient $\mathbf{H} = [A_1,\ B_1,\ C_1,\ D_1,\ A_2,\ B_2,\ C_2,\ D_2]$ yields the kth mode shape $\phi_n(x_n)$. Note that the coefficient $\mathbf{H}$ should be normalized through the mass normalization process to determine the normalized mode shape,

$$
\left[\begin{array}{c}
\int_{x_1=0}^{L_1} m_{a,1}(\phi_1(x_1))^2 dx_1 + \int_{x_2=0}^{L_2} m_{a,2}(\phi_2(x_2))^2 dx_2 \\[4pt]
+ M_t(\phi_2(L_2))^2 + 2M_t d_c\phi_2(L_2)\phi'_2(L_2) + J_t(\phi'_2(L_2))^2
\end{array}\right] = 1. \tag{14}
$$

Subsequently, the modal superposition method is used to derive the modal governing equation of the forced vibration of the ACR. The relative transverse vibration of the beam can be expressed as the summation of N truncated modes,

$$
w_{a,n}(x_n, t) = \sum_{k=1}^{N} \phi_{n,k}(x_n)\eta_k(t). \tag{15}
$$

Note that $\phi_{n,k}(x_n)$ is the kth mass normalized eigenmode ($k = 1, 2, \ldots, N$) for the beam section n. Based on the boundary conditions [Eq. (10)], orthogonality relations can be derived by

$$
\left[\begin{array}{c}
\int_{x_1=0}^{L_1} m_{a,1}\phi_{1,k}(x_1)\phi_{1,r}(x_1)dx_1 + \int_{x_2=0}^{L_2} m_{a,2}\phi_{2,k}(x_2)\phi_{2,r}(x_2)dx_2 + M_t\phi_{2,r}(L_2)\phi_{2,k}(L_2) \\[4pt]
+ M_t d_c\phi_{2,r}(L_2)\phi'_{2,k}(L_2) + M_t d_c\phi'_{2,r}(L_2)\phi_{2,k}(L_2) + J_t\phi'_{2,r}(L_2)\phi'_{2,k}(L_2)
\end{array}\right] = \delta_{kr},
$$

$$
\left[\begin{array}{c}
\int_{x_1=0}^{L_1} EI_{a,1}\dfrac{d^4\phi_{1,r}(x_1)}{dx_1^4}\dfrac{d\phi_{1,k}(x_1)}{dx_1}dx_1 + \int_{x_2=0}^{L_2} EI_{a,2}\dfrac{d^4\phi_{2,r}(x_2)}{dx_2^4}\dfrac{d\phi_{2,k}(x_2)}{dx_2}dx_2 \\[8pt]
- \phi_{2,k}(L_2)EI_{a,2}\dfrac{d^3\phi_{2,r}(x_2)}{dx_2^3}\bigg|_{x_2=L_2} + \dfrac{d\phi_{2,k}(x_2)}{dx_2}\bigg|_{x_2=L_2} EI_{a,2}\dfrac{d^2\phi_{2,r}(x_2)}{dx_2^2}\bigg|_{x_2=L_2}
\end{array}\right] = \Omega_r^2\delta_{kr},
\tag{16}
$$

where Ω_r is the natural frequency of the rth mode of the ACR. Substituting Eq. (15) into Eq. (2), multiplying by $\phi_{1,r}(x_1)$ and $\phi_{2,r}(x_2)$, integrating over each beam section, and applying Eq. (16) for simplification, the modal equation of the jth ACR can be derived as

$$
\ddot{\eta}_r(t) + 2\zeta_{a,r}\Omega_r\dot{\eta}_r(t) + \Omega_r^2\eta_r(t) = \chi_r\ddot{w}(\tilde{x}_j, t), \tag{17}
$$

where $\zeta_{a,r}$ is the introduced rth modal damping ratio. χ_r is expressed as

$$
\chi_r = \left[\begin{array}{c}
\int_{x_1=0}^{L_1} m_{a,1}\phi_{1,r}(x_1)dx_1 + \int_{x_2=0}^{L_2}(m_{a,2} + M_t\delta(x-L_2))\phi_{2,r}(x_2)dx_2 \\[4pt]
- \int_{x_2=0}^{L_2} M_t d_c\dfrac{d\delta(x_2-L_2)}{dx_2}\phi_{2,r}(x_2)dx_2
\end{array}\right]. \tag{18}
$$

Dividing Eq. (17) by $\phi_{2,r}(L_2)$, and letting $u_r(t) = \phi_{2,r}(L_2)\eta_r(t)$ yields

$$
M_r\ddot{u}_r(t) + C_r\dot{u}_r(t) + K_r u_r(t) = \alpha_r M_r\ddot{w}(\tilde{x}_j, t), \tag{19}
$$

where

$$
M_r = \frac{1}{\phi_{2,r}^2(L_2)}, \quad C_r = \frac{2\zeta_{a,r}\Omega_r}{\phi_{2,r}^2(L_2)},
$$

$$
K_r = \frac{\Omega_r^2}{\phi_{2,r}^2(L_2)}, \quad \alpha_r = \chi_r\phi_{2,r}(L_2). \tag{20}
$$

Equation (19) shows that the ACR can be equivalently represented as an equivalent lumped model. Notably, the continuous system represented by the ACR has an infinite number of vibrational modes, thus yielding an infinite number of SDOF systems with different parameters, where the subscript r denotes the rth mode. Additionally, a correction factor α_r should be introduced to correct the response of the lumped

03 August 2024 11:14:43

model. Since the natural frequency Ω_r and mode shape $\phi_{2,r}(L_2)$ vary as different NCR λ are applied, it is worth noting that all lumped parameters, including M_r, K_r, C_r, and α_r are λ-dependent. This is in contrast to Eq. (1), where only the equivalent stiffness varies as λ.

B. Theoretical model of graded metamaterial with ACRs

Based on the equivalent lumped model [i.e., Eq. (20)] for the ACR, the graded metamaterial with ACRs shown in Fig. 1(a) can be simplified as a graded metamaterial beam attached with resonators represented by lumped models. The main objective of this study is to achieve broadband vibration attenuation at low frequencies. Theoretically, only the low-frequency bandgap, predominantly contributed by the first-order mode of the ACR (i.e., $r = 1$), should be taken into consideration. However, although minimal, the influence of modes with $r > 1$ near the frequency Ω_1 (i.e., the fundamental natural frequency of the ACR) cannot be entirely disregarded as they may impact the prediction of the bandgap, particularly its upper limit, which will be observed in Sec. IV B. Here, the first three modes of the ACR (i.e., $r = 1, 2, 3$) are included in the analysis. Therefore, based on Eq. (20), the ACR is equivalent to a MDOF (Multi Degrees of Freedom) resonator (three resonators in total). Figure 3 depicts the schematic representation of the graded metamaterial integrated with the equivalent MDOF resonator. $2s + 1$ MDOF resonators are placed on the host beam at a lattice constant $d = L_b/(2s + 1)$, where the first resonator is $d/2$ from the clamped end. That is, resonators are placed in the middle of the unit cells. The jth ($j = 1$, $2,\ldots,2s + 1$) MDOF resonator corresponds to the jth ACR pair, which comprises three SDOF resonators corresponding to the first three modes of the ACR. It should be noted that the three SDOF resonators are conceptually attached to a shared point located within a unit cell.

Since the lattice constant is sufficiently smaller than the wavelength at low-frequency vibrations, the wave profile between the two adjacent unit cells can be approximated by a smooth function. Based on the averaging technique from the homogenization method,[51] it is reasonable to convert the concentrated reaction force of the SDOF resonator into a uniformly distributed force spaced by lattice constants, and its accuracy in different frequency regions has been confirmed in several works.[52,53] Under this assumption, the flexural wave propagation of the metamaterial beam attached with MDOF

resonators is governed by

$$EI_b \frac{\partial^4 w_{\text{rel}}(\tilde{x}, t)}{\partial \tilde{x}^4} + cI_b \frac{\partial^5 w_{\text{rel}}(\tilde{x}, t)}{\partial \tilde{x}^4 \partial t} + m_b \frac{\partial^2 w_{\text{rel}}(\tilde{x}, t)}{\partial t^2}$$
$$= -m_b \ddot{w}_b(t) + \sum_{r=1}^{3} \sum_{j=1}^{2s+1} 2M_{r,j}\Omega_{r,j}^2 u_{r,j}(t)\delta(\tilde{x} - \tilde{x}_j), \quad (21)$$

where $w_{\text{rel}}(\tilde{x}, t)$ is the relative transverse motion of the host beam, and $w_b(t)$ is the base excitation applied to the host beam. Thus, the absolute displacement of the host beam is $w(\tilde{x}, t) = w_b(t) + w_{\text{rel}}(\tilde{x}, t)$. $EI_b = E_b \frac{b_b h_b^3}{12}$ and $m_b = b_b \rho_b h_b$ are the bending stiffness and mass per length of the host beam, respectively. E_b, b_b, ρ_b, and h_b are Young's modulus, width, density, and thickness of the host beam, respectively. c is the equivalent strain rate damping coefficient, which can be expressed as $c = 2E_b\zeta_i/\omega_i$ with ζ_i and ω_i being the damping ratio and natural frequency of the ith mode of the host beam. $M_{r,j}\Omega_{r,j}^2 u_{r,j}(t)$ is the reaction force term exerted by the rth SDOF resonator in the jth MDOF resonator. Note that for the physical design, an ACR pair is placed symmetrically on either side of the host beam to maintain balance, as shown in Fig. 1(a). Consequently, in Eq. (21), the reaction force term should be doubled.

The motion equation of the rth SDOF resonator in the jth MDOF resonator is

$$\ddot{u}_{r,j}(t) + 2\zeta_a\Omega_{r,j}\dot{u}_{r,j}(t) + \Omega_{r,j}^2 u_{r,j}(t) = -\alpha_{r,j}\frac{\partial^2 w(\tilde{x}_j, t)}{\partial t^2}, \quad (22)$$

where the lumped parameters $\Omega_{r,j}$ and $\alpha_{r,j}$ in Eq. (22) will be determined by the grading strategies given in Sec. III C. Using the modal superposition method, the relative transverse motion $w_{\text{rel}}(\tilde{x}, t)$ is given by

$$w_{\text{rel}}(\tilde{x}, t) = \sum_{k=1}^{N} \Phi_k(\tilde{x})q_k(t) . \quad (23)$$

To avoid confusion with the symbols in the modeling of ACRs, $\Phi(\tilde{x})$ and $q(t)$ are used to represent the mode shape and the modal coordinate of the host beam. Applying Laplace transform to Eqs. (21) and (22), substituting the steady-state amplitude $\bar{u}_{r,j}$ and Eq. (23) into the Laplace form of Eq. (21) multiplying by $\Phi_i(\tilde{x})$, integrating over the host beam length from 0 to L_b, and then applying the orthogonality relations ($\int_0^{L_b} m_b\Phi_k(\tilde{x})\Phi_i(\tilde{x})d\tilde{x} = \delta_{ki}$; $\int_0^{L_b} EI_b \frac{d^4\Phi_k(\tilde{x})}{dx^4}\Phi_i(\tilde{x})d\tilde{x} = \omega_i^2\delta_{ki}$), we can obtain the modal governing
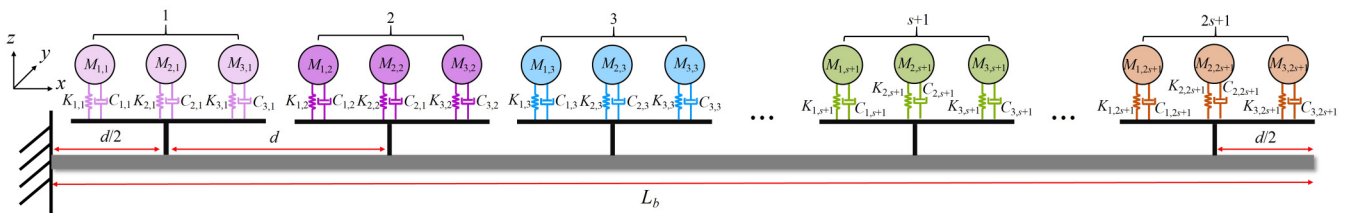

FIG. 3. Schematic of the graded metamaterial with MDOF resonators.

equation of the graded metamaterial,

$$\bar{q}_i + P_i \sum_{r=1}^{3} \left(\sum_{j=1}^{2s+1} P_{r,j} \Phi_i(\tilde{x}_j) \sum_{k=1}^{N} \Phi_k(\tilde{x}_j) \bar{q}_k \right) = \bar{f}_i, \quad (24)$$

where

$$P_i = \frac{\omega^2}{\omega_i^2 + 2i\omega\zeta_i\omega_i - \omega^2}, \quad P_{r,j} = \frac{2\alpha_{r,j}M_{r,j}\Omega_{r,j}^2}{\Omega_{r,j}^2 + 2i\omega\zeta_a\Omega_{r,j} - \omega^2}, \quad (25)$$

and

$$\bar{f}_i = P_i \frac{m_b a_{cc}}{\omega^2} \int_0^{L_b} \Phi_i(\tilde{x})dx + P_i \frac{a_{cc}}{\omega^2} \sum_{r=1}^{3} \sum_{j=1}^{2s+1} P_{r,j} \Phi_r(\tilde{x}_j). \quad (26)$$

In addition, $\bar{q}_i$ is the modal coordinate amplitude, and $a_{cc} = -\ddot{w}_b(t)/e^{i\omega t}$ is the acceleration amplitude of the base excitation. Rearranging Eq. (24) in the term of $\bar{q}_i$ gives

$$\mathbf{Cq} = \mathbf{F}, \quad (27)$$

where

$$\mathbf{C} = \begin{bmatrix} c_{11} & c_{12} & \dots & c_{1m} & \dots & c_{1N} \\ c_{21} & c_{22} & \dots & c_{2m} & \dots & c_{2N} \\ \dots & \dots & \dots & \dots & \dots & \dots \\ c_{i1} & c_{i2} & \dots & c_{im} & \dots & c_{iN} \\ \dots & \dots & \dots & \dots & \dots & \dots \\ c_{N1} & c_{N2} & \dots & c_{Nm} & \dots & c_{NN} \end{bmatrix} \mathbf{q} = \begin{bmatrix} \bar{q}_1 \\ \bar{q}_2 \\ \dots \\ \bar{q}_i \\ \dots \\ \bar{q}_N \end{bmatrix} \mathbf{F} = \begin{bmatrix} \bar{f}_1 \\ \bar{f}_2 \\ \dots \\ \bar{f}_i \\ \dots \\ \bar{f}_N \end{bmatrix} \quad (28)$$

and

$$c_{i,m} = \begin{cases} 1 - P_i \sum_{r=1}^{3} \sum_{j=1}^{2s+1} P_{r,j} \Phi_r(\tilde{x}_j) \Phi_m(\tilde{x}_j) & \text{for } m = i, \\ -P_i \sum_{r=1}^{3} \sum_{j=1}^{2s+1} P_{r,j} \Phi_r(\tilde{x}_j) \Phi_m(\tilde{x}_j) & \text{for } m \neq i. \end{cases} \quad (29)$$

By solving Eq. (27), the modal coordinate vector $\mathbf{q}$ can be obtained. Substituting the calculated $\mathbf{q}$ into Eq. (23) yields the steady-state amplitude $\bar{w}_{\rm rel}(\tilde{x})$ of the relative transverse vibration $w_{\rm rel}(\tilde{x}, t)$. The transmittance of the graded metamaterial can be obtained by

$$\tau = 20 \log_{10} \left(\frac{|\bar{w}_{\rm rel}(L_b) - a_{cc}/\omega^2|}{|-a_{cc}/\omega^2|} \right) \text{dB}. \quad (30)$$

In this work, $s = 4$, i.e., nine resonators are considered. The geometric and material properties used are given in Table I.

III. TUNING STRATEGY FOR AGGREGATED BAND

An aggregated band refers to a vibration attenuation region consisting of sequentially overlapped discrete bandgaps.[54] This study aims to create an aggregated band in the bending vibration of the graded metamaterial beam by assigning different NCR λ in the ACR shunt circuits according to a proper grading strategy. Before

TABLE I. Geometric and material properties of the proposed metamaterial.

Host beam	
Material	Steel
Length L_b	450 mm
Width b_b	20 mm
Thickness h_b	2 mm
Density p_b	7860 kg/m^3
Young's modulus E_b	200 GPa
Lattice constant d	50 mm
ACR (beam part)	
Material	Aluminum
Length L_s	40 mm
Width b	4 mm
Thickness h_s	0.8 mm
Density ρ_s	2700 kg/m^3
Young's modulus E_s	69 GPa
ACR (tip mass block)	
Material	Steel
Length L_a	5 mm
Width b_a	16 mm
Thickness h_a	16 mm
ACR (PZT patch)	
Material	PZT-5H
Length L_1	30 mm
Width b	4 mm
Thickness h_p	0.5 mm
Density ρ_p	7500 kg/m^3
Young's modulus $E_p^{\rm sc}$	60.6 GPa
Permittivity ε_{33}^S	2.5554×10^{-08} F/m
Piezoelectric constant d_{31}	-2.74×10^{-10} C/N
Electromechanical coupling coefficient k_{31}	0.3888

presenting the grading strategy, the tuning characteristics of the ACR by NC and the possible issues in implementing NC are first discussed.

A. Tuning characteristics of ACR by NC

The effect of the NC circuit on the effective modulus $E_p(\omega)$ of PZT has been widely studied.[42,44] As the equivalent parameters of the ACR are related to $E_p(\omega)$, it is necessary to briefly review how λ affects the effective modulus of PZT. Using the parameters outlined in Table I, Fig. 4 shows the normalized effective modulus of the PZT patch for different λ. As λ varies, it is observed that for $0 < \lambda < 1$, the effective modulus increases monotonically from the open-circuit modulus $E_p^{\rm oc}$ to positive infinity, indicating that PZT gets stiffer. On the other hand, for $1 < \lambda < \infty$, the effective modulus starts from negative infinity and increases to the short-circuit modulus $E_p^{\rm sc}$, implying that PZT gets softer. In other words, the two NCR ranges, i.e., $0 < \lambda < 1$ and $1 < \lambda < \infty$, correspond to the stiff and soft zones, respectively. Notably, the effective modulus of PZT becomes negative for $1 < \lambda < 1/(1 - k_{31}^2)$. Consequently, the overall effective bending stiffness of the ACR may also become negative, particularly as λ approaches 1, causing the system to lose
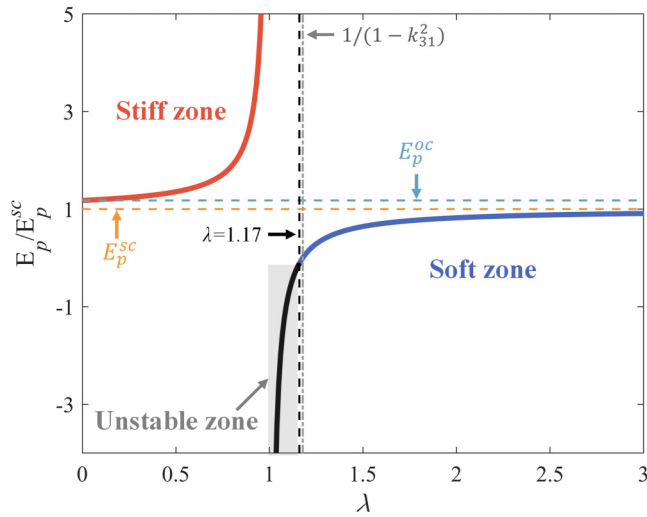
03 August 2024 11:14:43

FIG. 4. Effect of λ on the normalized effective modulus of PZT. Note that three zones, i.e., stiff, soft, and unstable zones, are defined according to different λ.

stability. To prevent this, a constraint $\lambda > 1.17$ is set to ensure that effective bending stiffness $EI_{a,1}$ remains positive. Accordingly, the region $1 < \lambda < 1.17$ refers to the unstable zone (i.e., the solid black line in Fig. 4).

Figure 5(a) shows the variation of the lumped parameters of the ACR with different λ. For simplicity, only the first mode $r = 1$

of the ACR is considered. The modal damping ratio $\zeta_{a,1}$ is assumed to be 0.005. It is found that M, K, and C increase with increasing λ in both the stiff and soft zones, except that the values decrease drastically when crossing the unstable zone.

B. Analysis of practical issues in the implementation of NC

Due to the active nature of NCs, some practical issues may arise during the implementation process, potentially affecting the reliability of the proposed ACR, and therefore, need to be specifically analyzed. The primary consideration should be the stability of the system. The stability of electro-mechanical systems with NC has been widely studied.[25,42] For composite beam structures with integrated PZT, it should be ensured that all poles of the system are on the left side of the Laplace domain. This constraint is satisfied as long as the effective bending stiffness of the composite segment is positive when $\omega = 0$,[25] which leads to the two stable zones in Fig. 4 ($0 < \lambda < 1$ and $1.17 < \lambda < \infty$). It is worth noting that, in practice, a resistor is usually connected in series or parallel to the NC to improve the circuit's robustness. To ensure that all poles are still on the left side of the Laplace domain, a negative resistance value is needed in one of the two stable branches of λ, depending on whether the series or parallel configuration is used.[25] In this case, it is recommended to use a programmable digital circuit to realize negative resistance.

In addition, for the analog circuit shown in Fig. 1(b) that implements the NC, the connection of the $+/-$ input pins of OP-AMP is related to the value of λ. Specifically, the connection shown in Fig. 1(b) applies to the case where $0 < \lambda < 1$. When
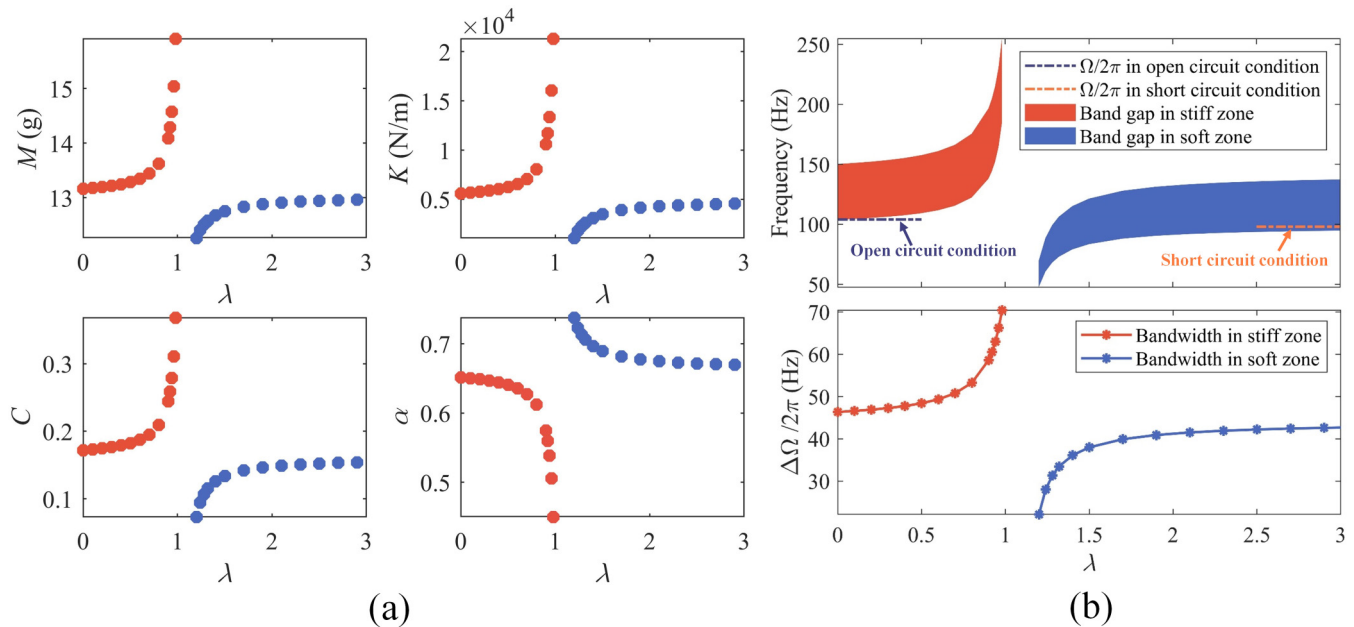

FIG. 5. (a) Effect of λ on the lumped parameters of the ACR and (b) bandgap variation with the change of λ. Variation of bandgap width with the change of λ is also plotted on (b).

$1.17 < \lambda < \infty$, the OP-AMP +/− input pins must be inverted to maintain stability.[42]

Furthermore, recall that the OP-AMP shown in Fig. 1(b) is assumed to be ideal. In practice, the circuit shown in Fig. 1(b) may require additional electronic components to address the bias currents and offset voltages caused by the non-ideal OP-AMP.[55] This will make the NC circuit no longer pure NC but behave as an NC connected to a parasitic inductor or resistor, causing the actual impedance to deviate from the desired value. To demonstrate that the proposed graded metamaterial system with ACRs remains effective in the presence of parasitic impedance, additional analyses were performed. Using the parameters outlined in Table I, Fig. 6 shows the variation of the normalized effective modulus $E_p(\omega)$ of PZT with frequency when the shunt circuit is the negative capacitor series parasitic inductor. λ is fixed at 0.8 and the inductance L is chosen as 0, 0.1, 30, and 50 H, respectively. It can be seen that for pure NC (i.e., $L = 0$ H), $E_p(\omega)$ remains constant at different frequencies. With the introduction of L, $E_p(\omega)$ gradually decreases to the open-circuit modulus E_p^{oc} as the frequency increases, and this tendency is more pronounced when L is large. This implies that if parasitic impedance is ignored, an inaccurate estimation of $E_p(\omega)$ will prevent the natural frequency of the ACR from being adjusted to the desired value. Fortunately, when L is small (e.g., $L = 0.1$ H), the decrease in $E_p(\omega)$ is almost negligible, especially in the low-frequency region, which is the frequency range of primary interest in this paper. This suggests that the proposed system is practically feasible as well. In addition, the effects of parasitic resistance will be discussed in conjunction with the transmittance results of the graded metamaterial system in Sec. V.

It is worth noting that the issues caused by the OP-AMP-based analog circuits can be circumvented by digital circuits. Recently, some 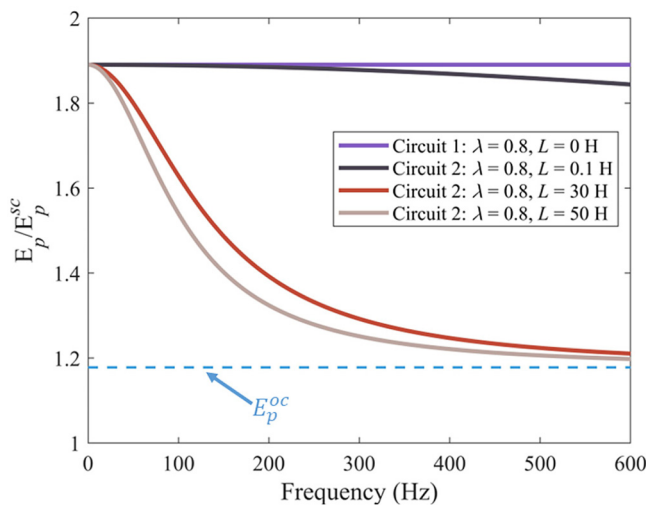researchers have suggested using digital circuits to design synthetic inductors, capacitors, and nonlinear capacitors.[56–58] The limitations of non-ideal OP-AMPs can be broken by writing discretized transfer functions in microprocessors to produce the same voltage-current characteristics as those under the action of actual electronic components. In this way, one can obtain the desired impedance.

C. Grading design

Note that the estimated bandgap edge frequency for the uniform metamaterial attached with identical SDOF resonators is[59]

$$\Omega_1 < \omega < \Omega_1\sqrt{\mu + 1}, \tag{31}$$

where $\mu = M/(m_b d)$ is the mass ratio. Ω_1 is the fundamental natural frequency of the ACR since only the bandgap in low frequency is considered. It is observed that the bandgap starts from Ω_1. Due to the correction factor α in Eq. (19), Eq. (31) requires a modification, which is expressed as follows:

$$\Omega_1 < \omega < \Omega_1\sqrt{\alpha\mu + 1}. \tag{32}$$

Based on Eq. (32), Fig. 5(b) displays the bandgap variation for different λ. It is found that the bandgap in the stiff zone starts from the resonance frequency of the ACR in the open-circuit condition and shifts to a high frequency with increasing λ. The bandgap in the soft zone starts from a low frequency and moves to the resonance frequency of the ACR in the short-circuit condition when $\lambda \to \infty$. It is noteworthy that the variation of bandgap width $\Delta\Omega = \Omega_1(\sqrt{\alpha\mu + 1} - 1)$ has a similar trend for different λ. Specifically, $\Delta\Omega$ is significantly larger in the stiff zone than in the soft zone. In particular, $\Delta\Omega$ becomes pretty narrow $\lambda \to 1.17$ from the right side. This is because the width of the bandgap depends on the additional mass ratio [i.e., μ in Eq. (32)],[59] while the equivalent mass M of ACRs is larger in the stiff zone than in the soft zone. Based on the above analyses, the grading profile of the proposed metamaterial beam is proposed.

A convenient approach to construct a graded metamaterial is to intentionally arrange the resonance frequency array of resonators in ascending or descending order with a constant frequency spacing. A dimensionless frequency spacing is defined as

$$\delta = \frac{\Omega_{1,j} - \Omega_{1,s+1}}{\Omega_{1,s+1}(j - (s+1))}, \tag{33}$$

where $\Omega_{1,j}$ and $\Omega_{1,s+1}$ is the fundamental natural frequency of the jth and the $(s+1)$th ACR, respectively, in which the $(s+1)$th ACR corresponds to the one mounted in the middle of the metamaterial beam. From Eq. (33), it can be inferred that +/− signs of δ correspond to the ascending/descending order of the natural frequency array. Based on the selection of $\Omega_{1,s+1}$ and δ, it can be found that to achieve the desired natural frequency array of the ACR, either the pure stiffening circuit ($0 < \lambda < 1$), the pure softening circuit ($1.17 < \lambda < \infty$), or the hybrid circuit is required. The following case study will discuss the broadband vibration attenuation performance of the metamaterial, considering the given grading profile.

FIG. 6. Variation of the normalized effective modulus of PZT with frequency for the case of a negative capacitor in series with a parasitic inductor. λ is fixed at 0.8 and the inductance L is chosen as 0, 0.1, 30, and 50 H, respectively.

IV. FINITE ELEMENT VERIFICATION

The purpose of this section is twofold: (1) to validate the equivalent lumped model for ACR and (2) to validate the developed graded metamaterials with ACRs. The validation was performed by the FE method.

A. Verification of equivalent lumped model

In this subsection, the ACR [Fig. 1(b)] is modeled by using COMSOL Multiphysics. Recall that the primary purpose of this study is to achieve a broad aggregated band within the low-frequency range by utilizing the concept of graded metamaterials, which heavily depends on the precision of tuning the ACR. Establishing an accurate ACR model lays the solid foundation for a dependable graded metamaterial model.

In the FE model of the ACR, one end is clamped, whereas the other end attached with the tip mass block remains free. The piezoelectric layer is implemented by the piezoelectric ceramic material PZT-5H, and the electrode coverage is realized by the terminal boundary condition. Use the circuit connections function in the electrical circuit module to connect the negative capacitor to the electrodes. A piezoelectric effect multiphysics module is implemented to the ACR to couple mechanical and electrical domains. A constant gravitational acceleration field, denoted as $a_{cc} = 9.8$ m/s^2, is applied to the ACR system. The geometric and material parameters of the ACR are listed in Table I. The NC circuits connected to the PZT patches are incorporated by the electrical module. Frequency domain analyses are also performed. For the equivalent lumped model, only the first mode of the ACR is considered for simplicity [i.e., $r = 1$ in Eq. (19)]. Figure 7(a) compares the fundamental natural frequency obtained from the FE and the lumped models for ACR's substrate of different lengths (i.e., L_s). Without loss of

generality, the NCR λ is set to zero (i.e., terminals of the PZT patches are set to open circuit). The corresponding relative errors $(\Omega_{\text{Theo}} - \Omega_{\text{FE}})/\Omega_{\text{FE}}$ are depicted in Fig. 7(a). The vibration modes of the ACR for the cases of $L_s = 40$ and 70 mm are superposed on the plot. It can be found that the maximum relative errors remain below 3.63%. As L_s increases, the accuracy of the equivalent lumped model improves. Particularly, $L_s = 80$ mm corresponds to an error of 1.01%. Many factors may cause the increased errors as the substrate of the ACR becomes shorter. For the relatively shorter beam, the size of the tip mass block will be large relative to the beam, which may lead to the incorrect estimation of the rotational inertia of the mass block, and may also compromise the validity of the mode shapes assumed in the theoretical model. Meanwhile, the relatively large size of the tip mass block may also affect the plane section assumption of the Euler beam. That is, the effect of shear deformation and rotary inertia of the beam's cross section may not be negligible. To further illustrate, Fig. 7(b) compares the natural frequency of the ACR predicted by the FE model and the equivalent lumped model with $L_s = 40$ mm and varying sizes of the tip mass block. The length, width, and height of the mass block are multiplied by a scaling ratio to reduce the size of the tip mass block. It can be seen that the natural frequency of ACRs gradually increases as the mass block size decreases. Meanwhile, the relative error gradually decreases (0.25% when the scaling ratio is 40%).

As mentioned in Sec. II, a relatively shorter beam is preferred due to the use of PZT. Hereafter, L_s is fixed at 40 mm, and the size of the tip mass block is not reduced (corresponding to an acceptable error of 3.63%). Figure 8(a) examines the fundamental natural frequency of the FE model and the equivalent lumped model as λ varies. The constraints $0 < \lambda < 1$ and $\lambda > 1.17$, respectively, corresponding to the stiff and soft zones, are considered. The relative errors $(\Omega_{\text{Theo}} - \Omega_{\text{FE}})/\Omega_{\text{FE}}$ are also depicted in Fig. 8(a). Positive
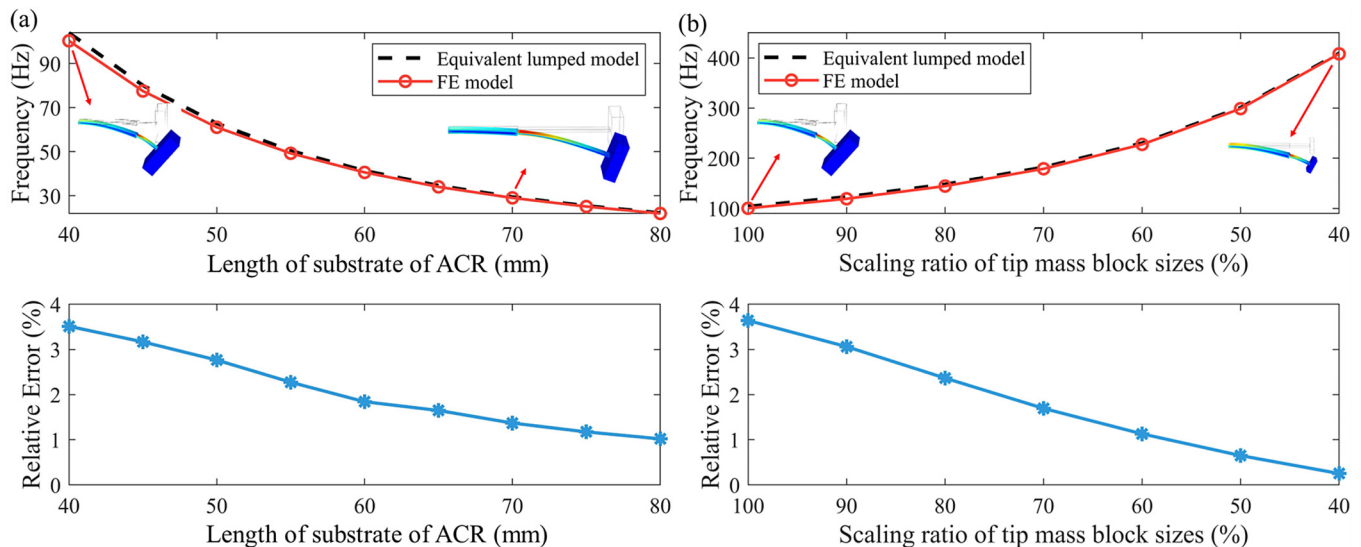
FIG. 7. Comparison of the fundamental natural frequency of ACRs predicted by the equivalent lumped model and the FE model in the cases of (a) varying the length of the substrate of ACR L_s; (b) varying the size of the tip mass block and the length of the substrate of ACR being set to 40 mm.
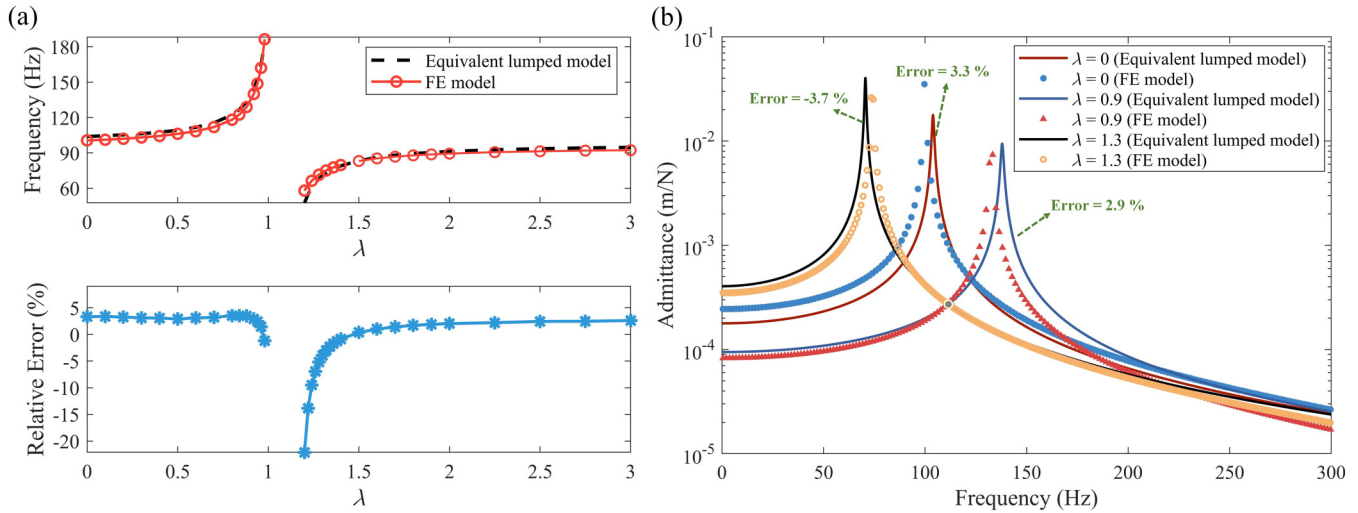
FIG. 8. (a) Comparison of the fundamental natural frequency of ACRs predicted by the equivalent lumped model and the FE model with varying λ and the length of the substrate of ACR L_s being set to 40 mm. (b) Comparison between the admittances calculated by the equivalent lumped model and the FE model for the cases of $\lambda = 0$, $\lambda = 0.9$, and $\lambda = 1.3$. The relative errors corresponding to these three cases are also marked.

errors indicate that the fundamental natural frequency predicted by the equivalent lumped mode is higher than that of the FE model, while the reverse is true for negative errors. It can be seen that the relative errors are positive when λ is far from the limit values l and 1.17. For this situation, the main error comes from the short beam setting (i.e., $L_s = 40$ mm), as discussed in the analysis of Fig. 7(a). Nevertheless, errors gradually change from positive to negative as λ approaches the limit value (i.e., $\lambda \to 1$ from the left side x axis and $\lambda \to 1.17$ from the right side x axis). In these cases, the fundamental natural frequencies predicted by the equivalent lumped model tend to be lower than that of the FE model in both the stiff and soft zones. This phenomenon can be attributed to the overestimation of capacitance C_p^S by the piezoelectric constitutive equation [i.e., Eq. (5)], which assumes fully clamped constraints of PZT. In the FE model, the capacitance of PZT is smaller than C_p^S due to their relatively loose constraints. According to the NCR $\lambda = -C_N/C_p^S$ defined in Sec. II A, the same λ implies that the negative capacitor value $|C_N|$ used in the FE model will be larger than actually needed. As $\lambda \to 1$ from the left side of the x axis, the relatively larger $|C_N|$ in the FE model contributes to a stiffer ACR, leading to a higher predicted natural frequency. Conversely, when $\lambda \to 1.17$ from the right side of the x axis, the relatively large $|C_N|$ in the FE model causes PZT to exhibit less softness compared to the equivalent lumped model, resulting in a higher predicted natural frequency for the ACR. Since the effective modulus change in PZT is more significant around the limit value of λ, the difference in the predicted natural frequency due to the misestimated capacitance will be more significant. Consequently, the FE model predicts a much higher natural frequency of the ACR, which leads to negative relative errors. Hereafter, to ensure sufficient accuracy, the constraint values of $\lambda = 0.98$ and $\lambda = 1.3$ are chosen for the stiff and soft zones, corresponding to errors of -1.2% and -3.7%,

respectively. To demonstrate more details, Fig. 8(b) presents the admittance of the substrate's tip of the ACR in the cases of $\lambda = 0$, $\lambda = 0.9$, and $\lambda = 1.3$. The results from both the equivalent lumped model and the FE model are plotted, where admittance based on the equivalent lumped model can be calculated by

$$A(\omega) = \frac{1}{M}\left[\frac{1}{(\Omega^2 - \omega^2)^2 + (2\zeta_a\omega\Omega)^2}\right]. \quad (34)$$

The relative errors related to these three cases are also marked in Fig. 8(b). From Fig. 8(b), it can be seen that the equivalent lumped model provides a good estimation in terms of fundamental natural frequency and displacement amplitude. As discussed before, when λ approaches the limit values, the fundamental natural frequency predicted by the FE model will be gradually higher than that of the equivalent lumped model, thus changing the error from positive to negative. This can be seen clearly in Fig. 8(b) for $\lambda = 1.3$. For the case of $\lambda = 0.9$, the error is still positive because λ is not close enough to the limit value 1.

B. Validation of metamaterial with MDOF resonators

After verifying the equivalent lumped model of the ACR, this subsection aims to verify the model of the metamaterial with MDOF resonators derived in Sec. II B. Recall that the first three modes of the ACR are considered. That is, the MDOF resonators consist of three SDOF resonators. In the FE model, the metamaterial consists of a steel beam with nine pairs of ACRs uniformly connected on both sides of the beam. The setup related to the ACR has been given in Sec. IV A. A base excitation is exerted on one end of the host beam while the other is free. A constant modal damping ratio $\zeta = 0.005$ is used for simplicity. The transmittance of the

metamaterial can be calculated by extracting the displacements at the free and clamped ends of the host beam. In addition, to obtain the band structure of the metamaterial in COMSOL, a unit cell consisting of a beam segment with a pair of ACRs attached to the middle of its sides is built. Floquet periodicity is applied to the beam segment to satisfy Bloch's theorem. One can obtain the band structure by scanning within the Brillouin zone and calculating the eigenfrequencies at different wave numbers. The geometric and material parameters of the metamaterial are given in Table I.

We commence with verifying the uniform metamaterial with identical MDOF resonators (i.e., $\delta = 0$). For the case of $\lambda = 0$, Fig. 9(a) compares the transmittances of the uniform metamaterial obtained by the analytical and FE models. The transmittance of 0 dB is depicted in Fig. 9(a) as a reference (dotted black line), where the range of the transmittance <0 dB is considered as the bandgap. To demonstrate the accuracy of the transmittance obtained by the FE method, Fig. 9(b) shows the band structure of one lattice of the metamaterial calculated by FE. Bloch's theorem is applied to describe the periodicity. According to the definition of the bandgap, the region between the two dispersion curves in Fig. 9(b) corresponds to the bandgap (gray shading). It can be seen that the gray area is consistent with the range where the transmittance is <0 dB, as shown in Fig. 9(a).

To demonstrate the validity of the modification made in the models, the result of the model that only considers the first mode of the ACR, referred to as the metamaterial with SDOF resonators, is depicted in Fig. 9(a). In addition, the transmittance obtained by the metamaterial model without considering the correction factor α in the equivalent SDOF model is also plotted in Fig. 9(a). For ease of description, we have renamed these metamaterial models as follows:

(1) Model A: Uniform metamaterial model with uncorrected SDOF resonators.
(2) Model B: Uniform metamaterial model with corrected SDOF resonators.
(3) Model C: Uniform metamaterial model with corrected MDOF resonators (as proposed in Sec. II B).

Since Models A–C are all based on Euler beam theory, they can only describe the bending modes. From Fig. 9(a), it can be seen that the onset frequency of the bandgap predicted by Models A–C is essentially the same, all of them differing slightly from that predicted by FE, which can be attributed to the error in the modeling of ACRs. Recalling Eq. (31), we know that the onset frequency of the bandgap predicted by Models A–C is equal to the natural frequency of the mass-spring resonator. We also know that the mass-spring resonator (i.e., the equivalent lumped model in this paper) is a simplified model of the ACR, whose modeling error has been discussed in detail in Sec. IV A. Therefore, the error in the onset frequency of the bandgap is highly dependent on the modeling error of the ACR. Another evidence is that the relative errors of the bandgap onset frequencies predicted by Models A–C are 3.64%, 3.69%, and 3.66%, respectively, which are very close to the modeling error of the ACR (3.63%) in Sec. IV A.

In contrast, the analytical results based on Models A and B exhibit significant errors at the cutoff frequency of the bandgap. The underlying reason is that, on the one hand, the correction factor α, which corrects the reaction force of the ACR, only has a notable impact on the cutoff frequency of the bandgap. On the other hand, the dynamic behavior of the metamaterial is dominated by the first-order mode of the ACR at frequencies below the first-order resonance frequency of the ACR. However, higher-order
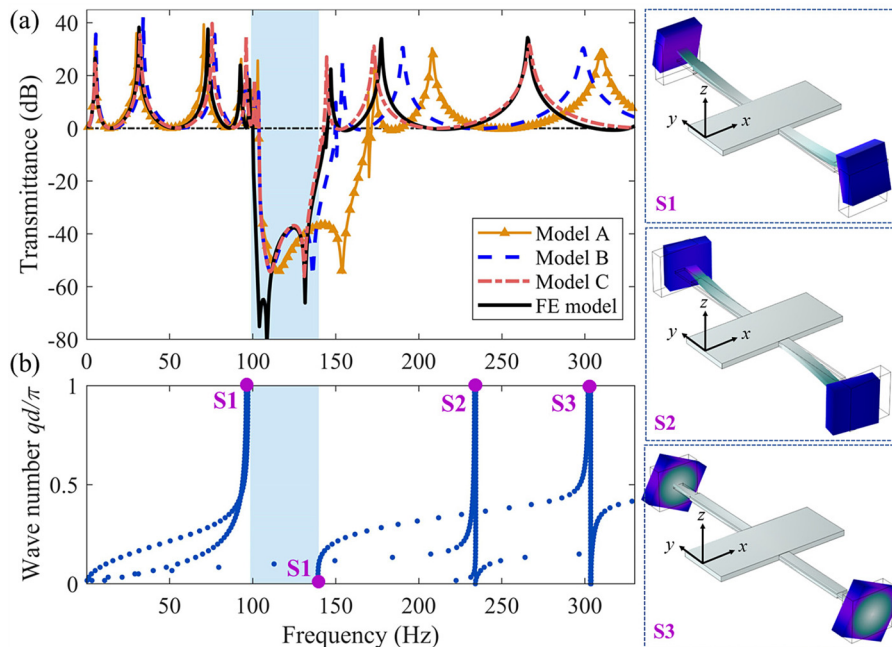

FIG. 9. (a) Transmittances of the uniform metamaterial calculated by analytical models A, B, C, and the FE model for $\delta = 0$ and $\lambda = 0$. Note that this case corresponds to the uniform metamaterial with the electromechanical resonators in the open-circuit condition. (b) Band structure of the metamaterial calculated by the FE model for $\delta = 0$ and $\lambda = 0$. The selected vibration modes of the unit cell are plotted.

modes of the ACR begin to dominate at frequencies above the first-order resonance frequency of the ACR, leading to errors in predicting the cutoff frequency of the bandgap and the subsequent mode peaks based on Models A and B. The relative errors in the bandgap's cutoff frequency predicted by Model C is 0.63%, reduced from 5.71% and 19.51% by Models A and B, respectively.

To get an insight into the vibration modes of the unit cell, three intrinsic points, namely, S1, S2, and S3, are extracted and presented in Fig. 9(b). The coupling between the bending vibration of the ACR and the host beam is observed in S1, resulting in the generation of the bandgap. S2 and S3 correspond to the lateral and torsional vibrations of the ACR, respectively, which do not contribute to the opening of bandgaps. This justifies considering only its bending vibration in the modeling of ACRs in Sec. II A. In addition, it should be noted that the higher-order bending modes of the ACR also lead to bandgaps but are beyond the scope of this paper due to their formation frequency at high frequencies. Interested readers can use the proposed method to analyze the bandgaps induced by the higher-order bending modes of ACRs.

Throughout this paper, the theoretical model referred to as Model C will be used. Figures 10 and 11 present the comparisons

of transmittances of the uniform metamaterial with resonators of identical properties ($\delta = 0$) obtained using both the theoretical and FE models, considering different λ in the stiff and soft zones, respectively. The band structures of the metamaterial regarding the corresponding cases are also plotted for reference, in which the blue shaded areas represent the bandgap. As anticipated, bandgap tuning follows the same trend as depicted in Fig. 5(b): when λ falls into the stiff zone, the bandgap shifts to higher frequencies and widens with increasing λ; in contrast, when λ is within the soft zone, the bandgap moves to lower frequencies and narrows with decreasing λ. Figures 10 and 11 clearly illustrate a high consistency between the theoretical and FE models.

Next, we validate the graded metamaterial. The fundamental natural frequency of the ACR by the middle, $f_{1,s+1}$, is set at 130 Hz. Two different values of δ, namely, 0.02 and 0.08, are considered. The desired resonance frequency array associated with ACRs can be determined according to Eq. (33). It should be noted that for $\delta = 0.02$, the desired resonance frequency array of ACRs falls into the stiff zone. Consequently, the stiffening circuit is employed. For $\delta = 0.08$, the desired resonance frequency array spans both the stiff and soft zones, implying the utilization of both stiffening and softening circuits (the hybrid circuit). The calculated
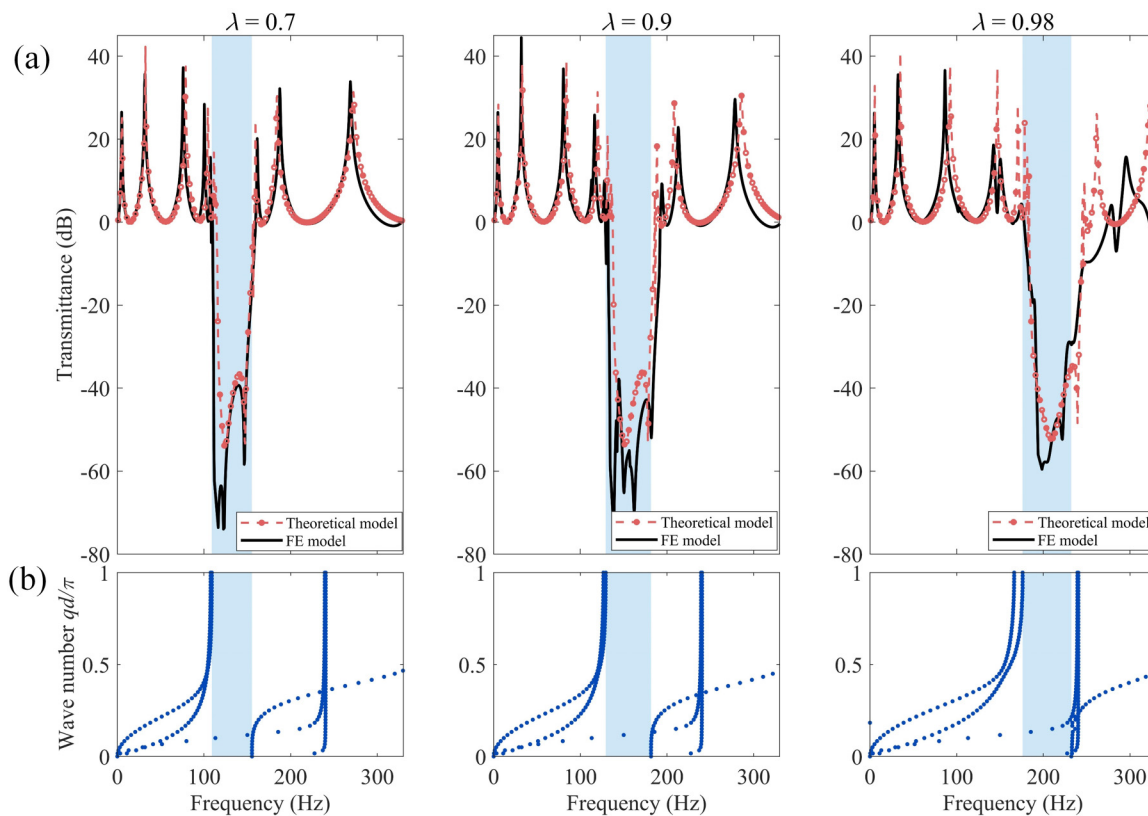

FIG. 10. (a) Comparisons of transmittances of the uniform metamaterial with identical resonators ($\delta = 0$) obtained by the theoretical and the FE models in the cases of different λ in the stiff zone. (b) Band structures of the metamaterial obtained by the FE model for the corresponding cases, where the bandgaps are shaded in blue.
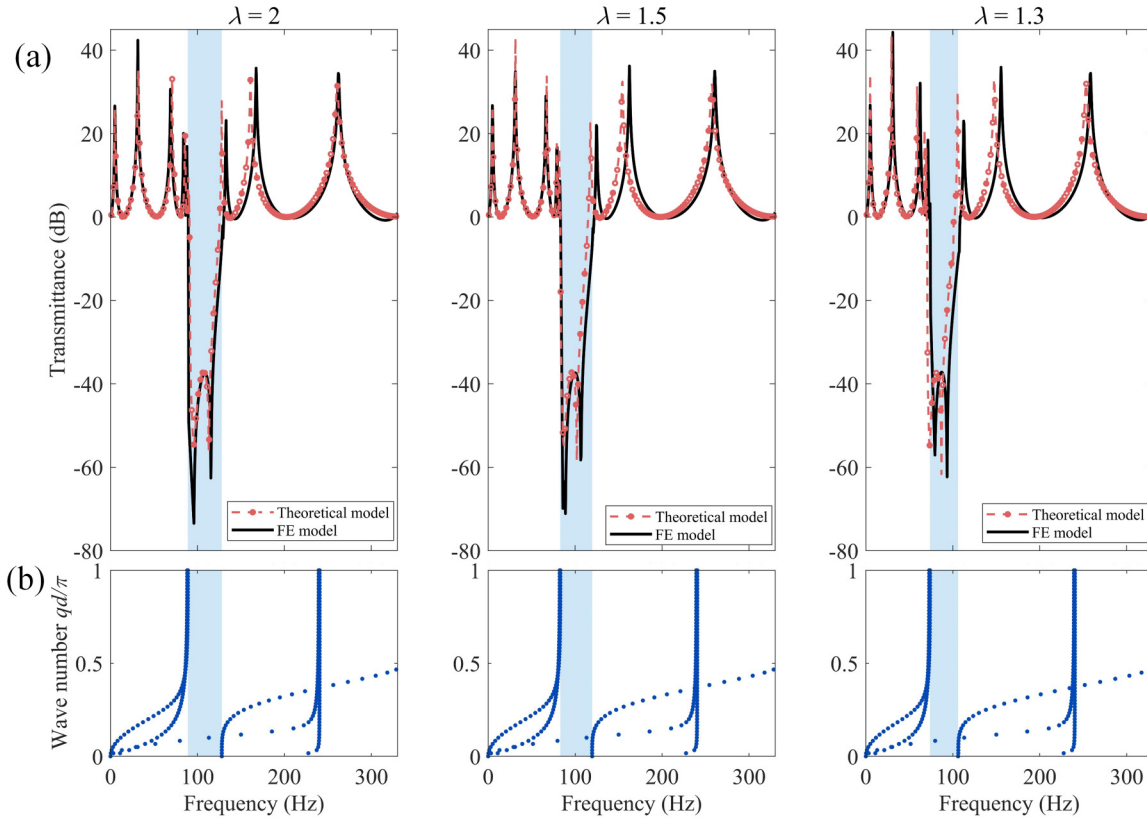
FIG. 11. (a) Comparisons of transmittances of the uniform metamaterial with identical resonators ($\delta = 0$) obtained by the theoretical and FE models in the cases of different λ in the soft zone. (b) Band structures of the metamaterial obtained by the FE model for the corresponding cases, where the bandgaps are shaded in blue.

λ in the respective ACRs can be determined using Eq. (11), as listed in Table II.

Figure 12 compares the transmittance of the graded metamaterial calculated by the theoretical and FE models, which show good agreement with each other. The transmittance of the uniform metamaterial obtained from the theoretical model when $\delta = 0$ and the natural frequency of the ACR which is 130 Hz is also plotted in Fig. 12 for comparison. It is observed that when δ is not 0, the vibration attenuation range becomes wider. In addition, for larger $\delta = 0.08$, which implies a more dispersed array of resonance frequencies of the ACRs, Fig. 12(b) shows that the vibration attenuation region of the theoretical result is in general agreement with that of the FE result, with slight discrepancies in the modal peaks within the attenuation region, especially at higher frequencies. This

is due to the modeling error of the ACR. In particular, as λ_8 and λ_9 in the ACR array, which correspond to the stiffening circuit, approach the limit value ($\lambda = 1$), this leads to an increase in the modeling error of the ACR at high frequencies. As a result, an increase in error at high frequencies can be observed in Fig. 12(b).

From Fig. 12(b), it can also be seen that the originally continuous bandgap is split into multiple discrete bandgaps due to the appearance of mode peaks within the attenuation region, the widest of which can be referred to as the main bandgap, as shown by the pink-colored region. For the discrete bandgaps in Fig. 12(b), it can be noticed that they are not uniform in width, with the last few discrete bandgaps being significantly wider than the previous ones. This is because the effective mass of the ACRs under grading varies, as discussed in Sec. III. To be specific, λ_7, λ_8, and λ_9 in the

TABLE II. Calculated NCR λ for the ACR array.

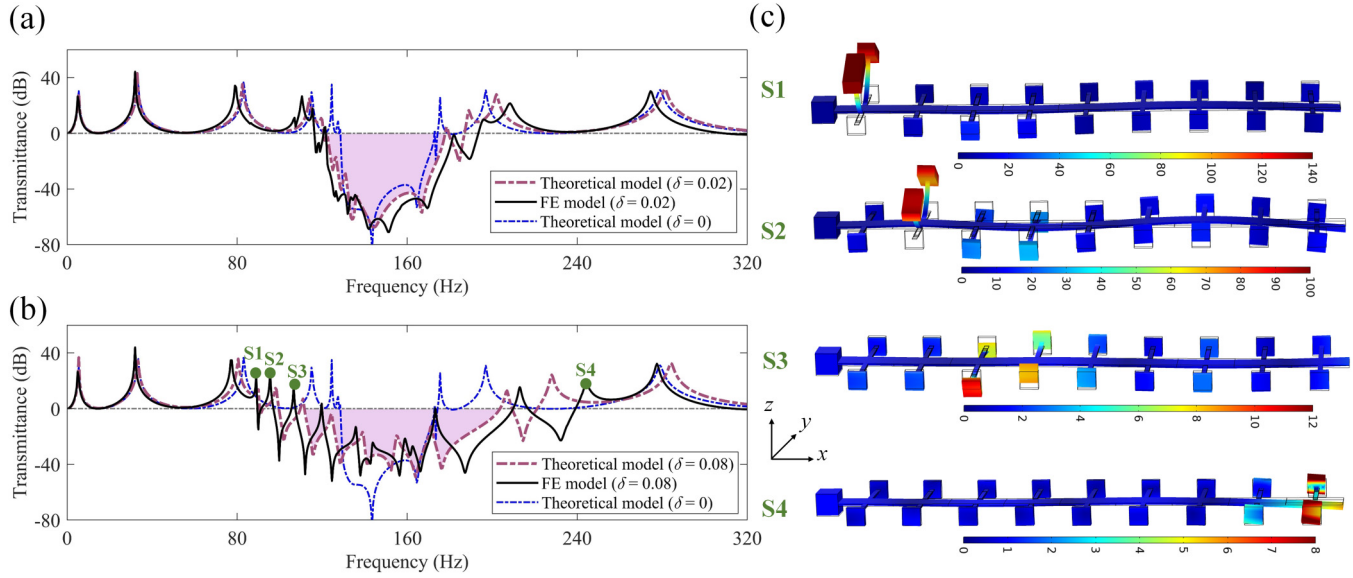| Case	λ_1	λ_2	λ_3	λ_4	λ_5	λ_6	λ_7	λ_8	λ_9
$\delta = 0.02$	0.766	0.798	0.821	0.843	0.859	0.872	0.885	0.899	0.908
$\delta = 0.08$	1.739	0	0.498	0.766	0.859	0.908	0.936	0.955	0.968

FIG. 12. Comparisons of transmittances of the graded metamaterial obtained by the theoretical and FE models with the case of (a) $f_{1,s+1} = 130$ Hz and $\delta = 0.02$ and (b) $f_{1,s+1} = 130$ Hz and $\delta = 0.08$. Note that the transmittance of the uniform metamaterial obtained by the theoretical model is also plotted for comparison. Subfigure (c) shows the vibration modes associated with the marked mode peaks S1, S2, S3, and S4 within the vibration attenuation region.

ACR array are closer to the limit value of 1 (as shown in Table II), causing the effective mass of these ACRs to be significantly larger than that of the others. Recalling Eq. (31), we know that the bandgap becomes wider as the resonator mass increases. Therefore, the seventh to ninth ACRs open wider discrete bandgaps.

Moreover, the vibration modes associated with the marked mode peaks (S1, S2, S3, and S4) are exacted and depicted in Fig. 12(c). It can be found that within the vibration attenuation region induced in the metamaterial beam, a distinct pattern of stress concentration, also called rainbow trapping, emerges. Initially, the stress concentration is observed in the ACR pair nearest to the clamped end of the host beam. As the frequency increases, this stress concentration sequentially propagates to the ACR pairs located toward the right end. These regions suffer higher deformation and stress levels than the surrounding areas, making the graded metamaterial suitable for broadband energy harvesting.[60] However, the large local deformation is undesirable for effective vibration attenuation.

In summary, the preceding discussion thoroughly validates the proposed graded metamaterial model, demonstrating its accuracy and reliability. In the following study, we are dedicated to achieving the optimal broadband attenuation performance of the graded metamaterial in the low-frequency range by properly tuning the ACRs via the grading strategy.

V. TUNING OF AGGREGATED BAND

This section commences with the effect of the parasitic resistance mentioned in Sec. III B on the dynamic response of the graded metamaterial. Building upon the findings from Ref. 54,

it was found that the resistance in the shunt circuit acts as electrical damping (electro-damping, for short), which can flatten resonant peaks within the attenuation region of the graded metamaterial. Our previous study[41] analyzed the complex band structure of piezoelectric metamaterials in the case of piezoelectric shunt circuits containing resistors and concluded that the imaginary part of wavenumbers will not be zero between the neighboring bandgaps, corroborating its ability to suppress localized resonance peaks. For a resistor R in series with the NC, the impedance of the shunt circuit is $Z = 1/(i\omega C_N) + R$. Note that the equivalent lumped model given by Eq. (19) is exclusively valid for a pure NC circuit, with real parameters M_r, K_r, and C_r. However, the presence of R in the shunt circuit yields a complex stiffness represented by real$\{K_r\}$ + imag$\{K_r\}$. Considering the complex form of K_r, the motion equation of the resonator based on the equivalent lumped model is modified by

$$\ddot{u}_{r,j}(t) + \underbrace{\left(2\zeta_a\Omega_{r,j} + \frac{\xi_{r,j}}{\omega}\right)}_{\text{Total damping}} \dot{u}_{r,j}(t) + \Omega_{r,j}^2 u_{r,j}(t) = -\alpha_{r,j}\frac{\partial^2 w(\tilde{x}_j, t)}{\partial t^2},$$

(35)

where $\xi_{r,j} = (\text{imag}\{K_{r,j}\})/M_{r,j}$ is the additional damping component induced by the resistance. The term $\xi_{r,j}/\omega$ implies that electro-damping is frequency-dependent. Equation (35) reveals that the introduction of R contributes to the increase of the overall damping of each resonator. Accordingly, $P_{r,j}$ [Eq. (25)] is modified by

$$P_{r,j} = \frac{2\alpha_{r,j}M_{r,j}\Omega_{r,j}^2}{\Omega_{r,j}^2 + i(2\omega\zeta_a\Omega_{r,j} + \xi_{r,j}) - \omega^2}.$$

(36)

In addition, an average transmittance is defined to characterize the intensity of the vibrational attenuation bands in a specific frequency range $[\omega_l, \omega_u]$,

$$\tau_{\text{avg}} = \frac{1}{\omega_u - \omega_l} \int_{\omega_l}^{\omega_u} \tau d\omega. \tag{37}$$

Figure 13 compares the transmittances of the graded metamaterial with $R = 0\,\Omega$ and $R = 2\,k\Omega$. The same $f_{1,s+1}$ and δ as in Fig. 12(b) are used. The bandgap ranges for the cases of $R = 0\,\Omega$ and $R = 2\,k\Omega$ are colored gray (120–209.5 Hz) and blue (107.5–239.5 Hz), respectively. A slight discrepancy between the theoretical model and the FE model can be observed. Referring to the error analysis in Fig. 9 in Sec. IV B, this discrepancy is due to modeling errors using ACRs with a relatively short substrate length. In addition, it is found that the bandgap is broadened with $R = 2\,k\Omega$. This is because when $R = 2\,k\Omega$, the resonant peaks are reduced to varying degrees, and some to less than zero dB. Particularly, the resonant peaks corresponding to the ACR pairs with λ far from its limit value (i.e., inside the green-dotted box) reduce slightly than those without resistance, suggesting that the additional electro-damping is relatively small. Conversely, the resonant peaks associated with the ACR pairs with λ close to the limit (i.e., inside the orange-dotted box) are almost flattened, indicating a significant electro-damping effect. However, the valley in the orange-dotted box undesirably disappears, signifying a diminished intensity of vibration attenuation. Furthermore, it can be deduced that when the resistance is too large, it opens the circuit, thus degrading the graded metamaterial into a uniform metamaterial. Based on Eq. (37), the average transmittance τ_{avg} within 107.5–239.5 Hz for the cases of $R = 0\,\Omega$ and $R = 2\,k\Omega$ are −21.5 and −16.4 dB, respectively, implying that higher resistances broaden the attenuation band while decreasing the attenuation intensity.

Several mode peaks in the FE result for the case of $R = 2\,k\Omega$ are labeled as S1, S2, S3, and S4 in Fig. 13, and the corresponding
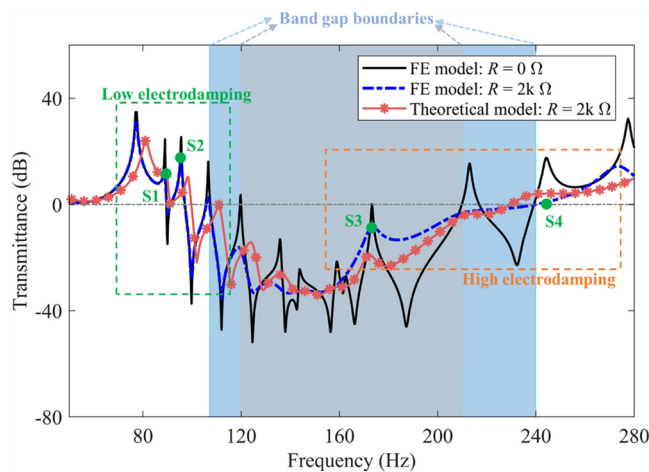

FIG. 13. Compassion of transmittances of the graded metamaterial with $R = 0\,\Omega$ and $R = 2\,k\Omega$ for the case of $f_{1,s+1} = 130$ Hz and $\delta = 0.08$.

mode shapes are shown in Fig. 14. It can be seen that the localized modes of the metamaterial beam remain for small electro-damping (i.e., S1 and S2), while the local modes disappear for large electro-damping (i.e., S3 and S4).

To gain insight into how electro-damping is affected by λ, Fig. 15 shows the variation of the electro-damping term $\xi_{1,j}$ for the first mode of the ACR with respect to j, considering different values of R. Two cases are considered. Case 1: $f_{1,s+1} = 130$ Hz, $\delta = 0.02$, and Case 2: $f_{1,s+1} = 105$ Hz, $\delta = 0.08$. The calculated λ in Cases 1 and 2 are listed in Table III.

The results in Fig. 15 show that electro-damping $\xi_{r,j}$ of the ACR exponentially increases as $\lambda \to 1$ from the left side of the x axis [i.e., $j \geq 3$ in Fig. 15(a), and $j \geq 5$ in Fig. 15(b)], and as $\lambda \to 1.17$ from the right side of the x axis [i.e., $j \leq 4$ in Fig. 15(b)]. Recall that $\xi_{r,j} = (\text{imag}\{K_{r,j}\})/M_{r,j}$. Therefore, the change in $\xi_{r,j}$ can be attributed to the effect of λ on the equivalent stiffness and mass of the ACR, which shows a similar trend as λ approaches the limit, as discussed in Sec. III. Furthermore, we can clearly see that the larger R is, the larger $\xi_{r,j}$ is, especially as λ is close to the limit. Based on these previous results, it is reasonable to conclude that the varying resistance is ideal in the ACR array of graded metamaterials for better vibration suppression performance. When λ in the ACR is far from the limit, a large resistance ensures sufficient electro-damping to reduce the resonance peaks, and when λ approaches the limit, a small resistance can avoid excessive weakening of the vibration suppression strength. The optimization method proposed in our previous work[39] can be used to determine the optimal resistance value of each ACR. However, since this is not the focus of this paper, a fixed $R = 500\,\Omega$ in series with the NC circuit is set to ensure proper electro-damping.

To investigate the impact of different configurations of the NC circuit on achieving an aggregated band when δ is varying, we consider three cases: the softening circuit (Case 1), the stiffening circuit (Case 2), and the hybrid circuit (Case 3). In Sec. IV, the verification process leads us to select appropriate values of λ for the stiffening and softening circuits, namely, (0, 0.98) and (1.3, +∞), respectively, These values correspond to the fundamental natural frequencies of the ACR, which are (103.92 Hz, 184.19 Hz) and (70.63 Hz, 97.84 Hz). For the grading strategy given in Eq. (33), it is reasonable to set $f_{1,s+1}$ to the center frequency of the adjustable range, i.e., 144, 84, and 127 Hz for Cases 1–3, respectively. Based on the above scenarios, the thresholds of δ for Cases 1–3 should be (0, 0.038), (0, 068), and (0, 0.110), respectively. Figures 16(a)–16(c) display the evolution of the attenuation region, indicated by the blue-colored area where transmittance is less than 0 dB, as the grading coefficient δ varies.

Generally, the introduction of grading leads to a broader aggregated band. However, the widening of the vibration attenuation zone achieved through the grading ACRs based on the softening circuit (i.e., Case 1) is noticeably less effective than the other two cases. This is attributed to the relatively large error under the softening circuit, making the effective range of λ relatively smaller (as depicted in Fig. 8), which restricts the adjustable bandgap range available through the softening circuit.

In contrast, the hybrid configuration (Case 3) allows for a wider range of attenuation zone adjustment because it combines the natural frequency tuning range of the ACR in both the
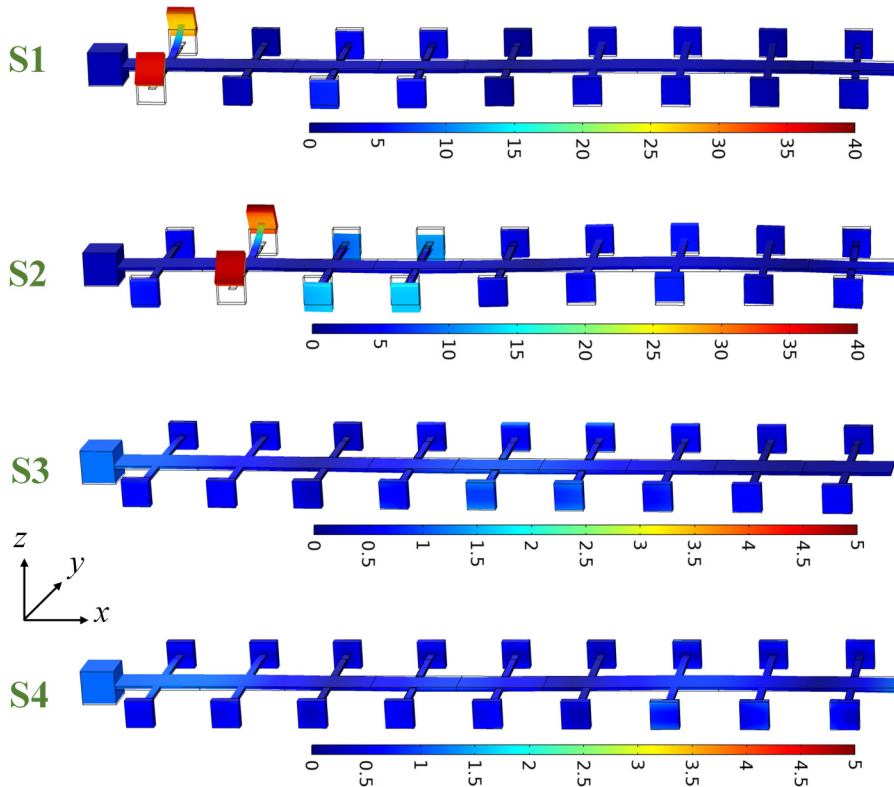
FIG. 14. The vibration modes associated with the marked mode peaks S1, S2, S3, and S4 in Fig. 12.
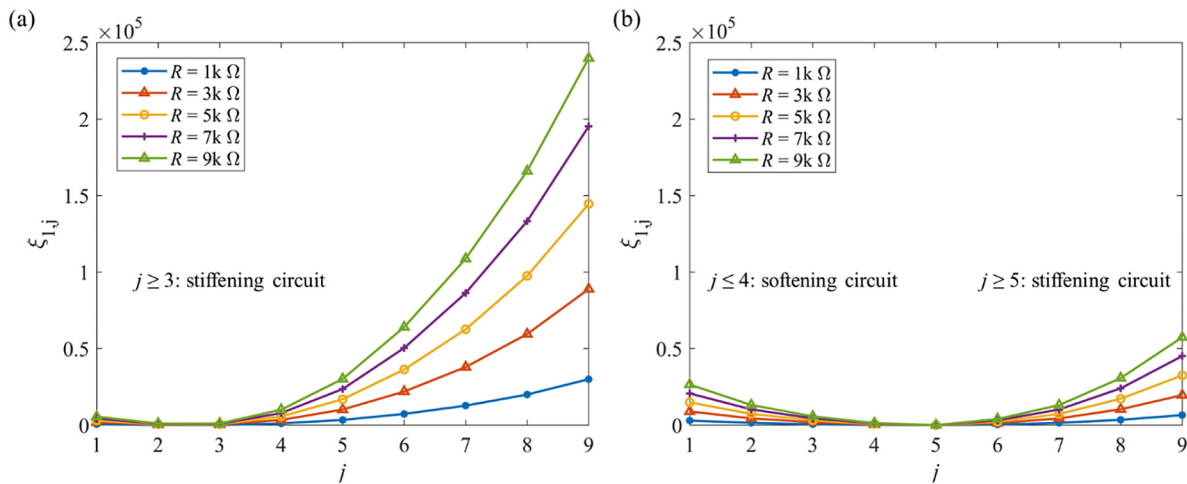
FIG. 15. Variation of the electro-damping term ξ_{1j} for the first mode of the ACR with respect to j with (a) Case 1 and (b) Case 2.

TABLE III. Calculated NCR λ of the ACR array in Cases 1 and 2.

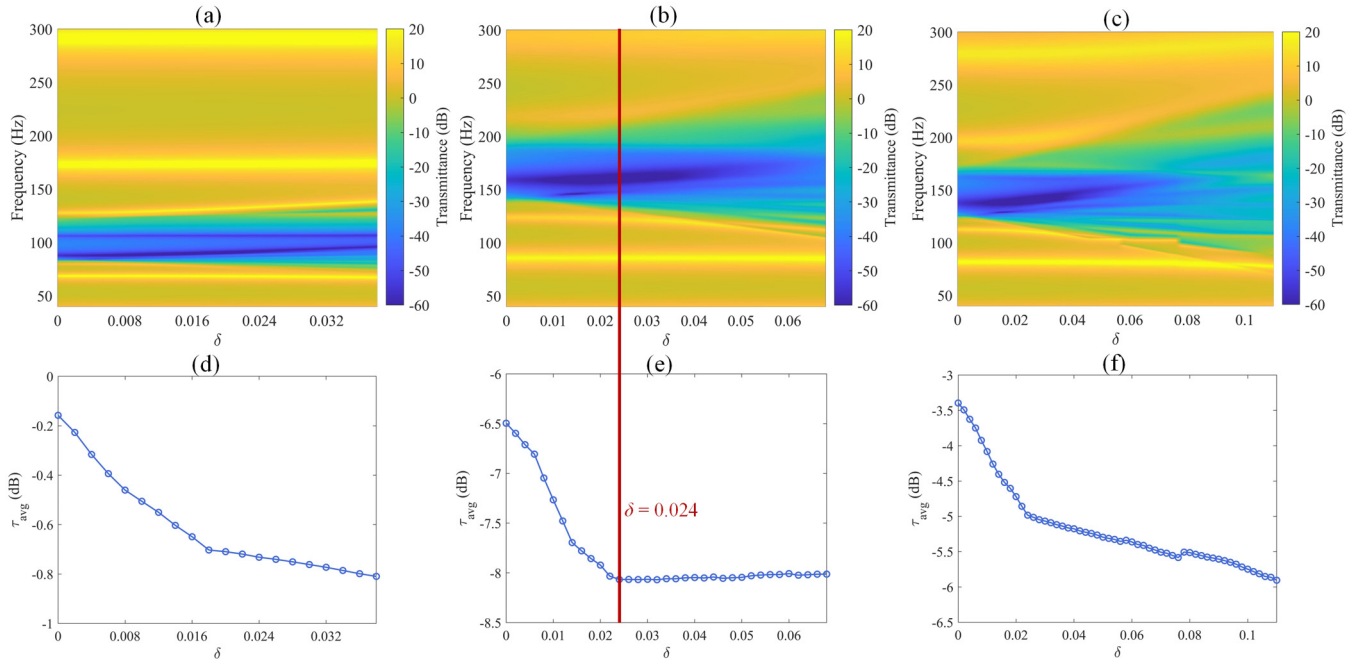| Case	λ_1	λ_2	λ_3	λ_4	λ_5	λ_6	λ_7	λ_8	λ_9
Case 1	1.739	0	0.498	0.766	0.859	0.908	0.936	0.955	0.968
Case 2	1.305	1.451	1.839	5.633	0.183	0.676	0.799	0.868	0.907

FIG. 16. The vibration attenuation heatmaps with varying δ: (a) Case 1; (b) Case 2; and (c) Case 3. Evolution of the average transmittance over the frequency range of interest with varying δ: (d) Case 1; (e) Case 2; and (f) Case 3.

softening and stiffening cases, resulting in a broader aggregated band. Figure 17 shows the transmittance of the graded metamaterial using the hybrid configuration with $\delta = 0.1$. The case with open-circuited ACR is also plotted for comparison. It is evident
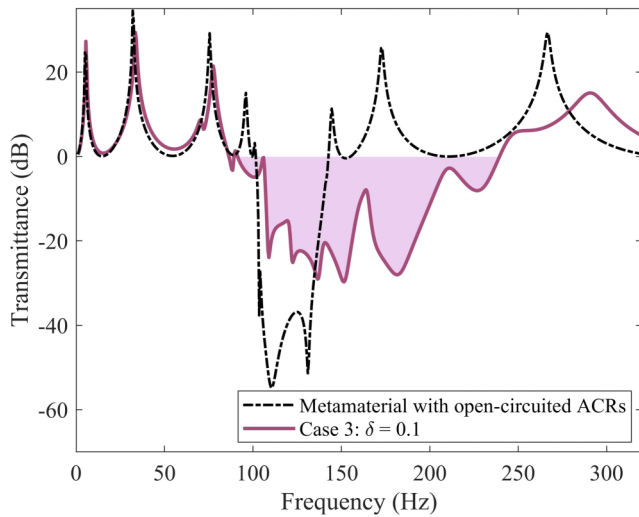

FIG. 17. Transmittances for the graded metamaterial using the hybrid configuration with $\delta = 0.1$. The transmittance for the metamaterial with open-circuited ACRs (black dotted line) is plotted for comparison.

that a wider aggregated band (indicated by pink area) in the graded metamaterial, spanning 86.4–239.5 Hz, is 272.5% wider than the reference case (101.6–142.7 Hz). Moreover, the effect of δ on the average transmittance τ_{avg} over the frequency range of interest (50–300 Hz is selected here) is investigated for different configurations of the NC circuit (i.e., Cases 1–3), as shown in Figs. 16(d)–16(f). Specifically, Fig. 16(e) shows that τ_{avg} decreases with increasing δ until it approaches a limiting value (approximately −8 dB) when $\delta > 0.024$. Conversely, Figs. 16(d) and 16(f) show a consistent decrease in τ_{avg} with increasing δ, indicating an enhancement in vibration attenuation intensity within the 50–300 Hz range. The limiting values are not reached in Figs. 16(d) and 16(f), probably because the range of λ is conservative in the softening circuit. In addition, it is crucial to emphasize that although the broadening of the vibration attenuation band is most effective in Case 3 (the hybrid circuit), it does not possess the highest level of attenuation intensity. To be precise, Case 2 exhibits the lowest τ_{avg}, whereas Case 1 has the highest. This is because the attenuation band in Case 2 is located at a higher frequency. It is known that the attenuation intensity of the bandgap gradually increases as it moves to higher frequencies, which is why it is more difficult to attenuate the vibration at lower frequencies. The proposed metamaterial in this paper could be further refined by integrating the adaptive function into the ACR through digital circuits. Such integration would facilitate automatic updating of the grading pattern in response to the changes in ambient vibration spectra, thereby effectively broadening the operational bandwidth of the system.

VI. CONCLUSIONS

This paper presents a novel graded metamaterial that enables effective vibration control across a wide range of low frequencies. An actively controllable resonator array composed of piezoelectric cantilever beams with tip mass blocks and connected to negative capacitance circuits is mounted to the host beam. With a proposed grading strategy, the ACR array can be finely tuned to the desired grading pattern by modifying the NC of the shunt circuits. To ensure accurate tuning, the ACR is first simplified to an equivalent lumped model with a correction factor. The variation of the equivalent parameters of the ACR with NC is investigated. It is found that a significant change in the dynamic equivalent mass affected by NC results in the expansion or shrinkage of the bandgap. Subsequently, the effect of NC on bandgap tuning is corroborated by a theoretical model and validated using a finite element model. The theoretical and finite element results exhibit a high level of agreement, except for cases where the NC is close to the limit value, which arises due to the misestimation of the inherent capacitance of the piezoelectric transducer. A reliable range of NC with relative errors within 3.0% is suggested. After that, the impact of bandgap widening under the grading pattern of the ACR array is investigated. It is found that the grading strategy employing a stiffening circuit enlarges the vibration attenuation zone more significantly as compared to the softening circuit. However, the more scattered bandgaps introduce wave localization when using the stiffening circuit. An equivalent additional damping caused by the resistance is derived to mitigate this effect, which exponentially increases as the NC approaches the limit value. This additional damping helps us significantly to alleviate wave localization. In an optimal scenario with proper NC and resistance, it is demonstrated that the graded metamaterial achieves a broadband vibration attenuation region in the low-frequency range, which is 272.5% wider than that of the uniform metamaterial with open-circuited ACRs.

ACKNOWLEDGMENTS

AUTHOR DECLARATIONS

Conflict of Interest

The authors have no conflicts to disclose.

Author Contributions

Yupei Jian: Conceptualization (equal); Formal analysis (equal); Investigation (equal); Methodology (equal); Validation (equal); Writing – original draft (equal); Writing – review & editing (equal). **Guobiao Hu:** Conceptualization (equal); Methodology (equal); Writing – original draft (equal). **Lihua Tang:** Conceptualization (equal); Formal analysis (equal); Supervision (equal). **Jiawen Xu:** Methodology (equal); Writing – original draft (equal). **Deqing Huang:** Conceptualization (equal); Supervision (equal). **Kean Aw:** Conceptualization (equal); Supervision (equal).

DATA AVAILABILITY

The data that support the findings of this study are available within the article.

REFERENCES

[1] M. Arif, M. Asif, and I. Ahmed, "Advanced composite material for aerospace application—A review," Int. J. Eng. Manuf. Sci. **7**(2), 393–409 (2017).

[2] W. Zhang and J. Xu, "Advanced lightweight materials for automobiles: A review," Mater. Des. **221**, 110994 (2022).

[3] A. Manalo, T. Aravinthan, A. Fam et al., "State-of-the-art review on FRP sandwich systems for lightweight civil infrastructure," J. Compos. Constr. **21**(1), 04016068 (2017).

[4] S. Wang, H. Zheng, L. Tang et al., "Vibration-based and computer vision-aided nondestructive health condition evaluation of rail track structures," J. Civil Struct. Health Monit. **13**(1), 1–14 (2023).

[5] K. Liu and J. Liu, "The damped dynamic vibration absorbers: Revisited and new result," J. Sound Vib. **284**(3-5), 1181–1189 (2005).

[6] Z. Shu, R. You, and Y. Zhou, "Viscoelastic materials for structural dampers: A review," Constr. Build. Mater. **342**, 127955 (2022).

[7] M. Nouh, O. Aldraihem, and A. Baz, "Wave propagation in metamaterial plates with periodic local resonances," J. Sound Vib. **341**, 53–73 (2015).

[8] W. Zhang, R. Neville, D. Zhang et al., "The two-dimensional elasticity of a chiral hinge lattice metamaterial," Int. J. Solids Struct. **141**, 254–263 (2018).

[9] M. I. Hussein, M. J. Leamy, and M. Ruzzene, "Dynamics of phononic materials and structures: Historical origins, recent progress, and future outlook," Appl. Mech. Rev. **66**(4), 040802 (2014).

[10] X. An, X. Yuan, G. Sun et al., "Sandwich plate-type metastructures with periodic graded resonators for low-frequency and broadband vibration attenuation," Ocean Eng. **298**, 117229 (2024).

[11] F. A. Pires, L. Sangiuliano, H. Denayer et al., "The use of locally resonant metamaterials to reduce flow-induced noise and vibration," J. Sound Vib. **535**, 117106 (2022).

[12] G. Ji and J. Huber, "Recent progress in acoustic metamaterials and active piezoelectric acoustic metamaterials—A review," Appl. Mater. Today **26**, 101260 (2022).

[13] B. I. Popa, D. Shinde, A. Konneker et al., "Active acoustic metamaterials reconfigurable in real time," Phys. Rev. B **91**(22), 220303 (2015).

[14] A. Bacigalupo, M. L. De Bellis, and D. Misseroni, "Design of tunable acoustic metamaterials with periodic piezoelectric microstructure," Extreme Mech. Lett. **40**, 100977 (2020).

[15] F. Casadei, T. Delpero, A. Bergamini et al., "Piezoelectric resonator arrays for tunable acoustic waveguides and metamaterials," J. Appl. Phys. **112**(6), 064902 (2012).

[16] Z. Chen, S. Sun, L. Deng et al., "Investigation of a new metamaterial magneto-rheological elastomer isolator with tunable vibration bandgaps," Mech. Syst. Signal Process. **170**, 108806 (2022).

[17] C. L. Willey, V. W. Chen, K. J. Scalzi et al., "A reconfigurable magnetorheological elastomer acoustic metamaterial," Appl. Phys. Lett. **117**(10), 104102 (2020).

[18] V. Candido de Sousa, D. Tan, C. De Marqui et al., "Tunable metamaterial beam with shape memory alloy resonators: Theory and experiment," Appl. Phys. Lett. **113**(14), 143502 (2018).

[19] K. C. Chuang, X. F. Lv, and Y. H. Wang, "A bandgap switchable elastic metamaterial using shape memory alloys," J. Appl. Phys. **125**(5), 055101 (2019).

[20] H. Zhang, Y. Xiao, J. Wen et al., "Ultra-thin smart acoustic metasurface for low-frequency sound insulation," Appl. Phys. Lett. **108**(14), 141902 (2016).

[21] X. Zhang, F. Chen, Z. Chen et al., "Membrane-type smart metamaterials for multi-modal sound insulation," J. Acoust. Soc. Am. **144**(6), 3514–3524 (2018).

[22] M. Wang, K. Yi, and R. Zhu, "Tunable underwater low-frequency sound absorption via locally resonant piezoelectric metamaterials," J. Sound Vib. **548**, 117514 (2023).

03 August 2024 11:14:43

[23]W. Tian, T. Zhao, and Z. Yang, "Theoretical modelling and design of metamaterial stiffened plate for vibration suppression and supersonic flutter," Compos. Struct. **282**, 115010 (2022).

[24]L. Tang, X. Yao, G. Wu et al., "Band gaps and vibration attenuation characteristics analysis in homogeneous beam coupled with periodic oscillators based on the method of reverberation-ray matrix," Front. Mater. **9**, 848323 (2022).

[25]K. Yi and M. Collet, "Broadening low-frequency bandgaps in locally resonant piezoelectric metamaterials by negative capacitance," J. Sound Vib. **493**, 115837 (2021).

[26]Z. Yaw, W. Zhou, and C. W. Lim, "Anomalous wave control by an adaptive elastic metasurface shunted with negative capacitance circuit," J. Sound Vib. **525**, 116782 (2022).

[27]S. B. Chen, J. H. Wen, D. L. Yu et al., "Band gap control of phononic beam with negative capacitance piezoelectric shunt," Chin. Phys. B **20**(1), 014301 (2011).

[28]B. Bao, M. Lallart, and D. Guyomar, "Manipulating elastic waves through piezoelectric metamaterial with nonlinear electrical switched dual-connected topologies," Int. J. Mech. Sci. **172**, 105423 (2020).

[29]B. Bao, M. Lallart, and D. Guyomar, "Structural design of a piezoelectric metastructure with nonlinear electrical Bi-link networks for elastic wave control," Int. J. Mech. Sci. **181**, 105730 (2020).

[30]X. Zhang, H. Yu, Z. He et al., "A metamaterial beam with inverse nonlinearity for broadband micro-vibration attenuation," Mech. Syst. Signal Process. **159**, 107826 (2021).

[31]G. Hu, A. C. M. Austin, V. Sorokin et al., "Metamaterial beam with graded local resonators for broadband vibration suppression," Mech. Syst. Signal Process. **146**, 106982 (2021).

[32]J. Yao, R. Sun, F. Scarpa et al., "Two-dimensional graded metamaterials with auxetic rectangular perforations," Compos. Struct. **261**, 113313 (2021).

[33]A. Banerjee, R. Das, and E. P. Calius, "Frequency graded 1D metamaterials: A study on the attenuation bands," J. Appl. Phys. **122**(7), 075101 (2017).

[34]C. Liu and C. Reina, "Broadband locally resonant metamaterials with graded hierarchical architecture," J. Appl. Phys. **123**(9), 095108 (2018).

[35]L. Zhao and S. Zhou, "Compact acoustic rainbow trapping in a bioinspired spiral array of graded locally resonant metamaterials," Sensors **19**(4), 788 (2019).

[36]H. Meng, D. Chronopoulos, A. T. Fabro et al., "Optimal design of rainbow elastic metamaterials," Int. J. Mech. Sci. **165**, 105185 (2020).

[37]M. Alshaqaq and A. Erturk, "Graded multifunctional piezoelectric metastructures for wideband vibration attenuation and energy harvesting," Smart Mater. Struct. **30**(1), 015029 (2020).

[38]Y. Liu, C. Han, and D. Liu, "Broadband vibration suppression of graded/disorder piezoelectric metamaterials," Mech. Adv. Mater. Struct. **30**(4), 710–723 (2023).

[39]Y. Jian, L. Tang, G. Hu et al., "Adaptive genetic algorithm enabled tailoring of piezoelectric metamaterials for optimal vibration attenuation," Smart Mater. Struct. **31**(7), 075026 (2022).

[40]R. L. Thomes, J. A. Mosquera-Sánchez, and C. De Marqui, "Bandgap widening by optimized disorder in one-dimensional locally resonant piezoelectric metamaterials," J. Sound Vib. **512**, 116369 (2021).

[41]Y. Jian, G. Hu, L. Tang et al., "Analytical and experimental study of a metamaterial beam with grading piezoelectric transducers for vibration attenuation band widening," Eng. Struct. **275**, 115091 (2023).

[42]M. Berardengo, O. Thomas, C. Giraud-Audine et al., "Improved resistive shunt by means of negative capacitance: New circuit, performances and multi-mode control," Smart Mater. Struct. **25**(7), 075033 (2016).

[43]M. Date, M. Kutani, and S. Sakai, "Electrically controlled elasticity utilizing piezoelectric coupling," J. Appl. Phys. **87**(2), 863–868 (2000).

[44]P. Mokrý, E. Fukada, and K. Yamamoto, "Sound absorbing system as an application of the active elasticity control technique," J. Appl. Phys. **94**(11), 7356–7362 (2003).

[45]Y. Chen, G. Huang, and C. T. Sun, "Band gap control in an active elastic metamaterial with negative capacitance piezoelectric shunting," J. Vib. Acoust. **136**(6), 061008 (2014).

[46]S. A. R. Kuchibhatla and M. J. Leamy, "Numerical demonstration of a topologically-protected electroacoustic transistor," Front. Acoust. **1**, 1251215 (2023).

[47]S. El-Borgi, R. Fernandes, P. Rajendran et al., "Multiple bandgap formation in a locally resonant linear metamaterial beam: Theory and experiments," J. Sound Vib. **488**, 115647 (2020).

[48]X. Li, Y. Chen, G. Hu et al., "A self-adaptive metamaterial beam with digitally controlled resonators for subwavelength broadband flexural wave attenuation," Smart Mater. Struct. **27**(4), 045015 (2018).

[49]C. Sugino, S. Leadenham, M. Ruzzene et al., "An investigation of electroelastic bandgap formation in locally resonant piezoelectric metastructures," Smart Mater. Struct. **26**(5), 055029 (2017).

[50]N. W. Hagood and A. Von Flotow, "Damping of structural vibrations with piezoelectric materials and passive electrical networks," J. Sound Vib. **146**(2), 243–268 (1991).

[51]J. Lou, X. Fang, J. Du et al., "Propagation of fundamental and third harmonics along a nonlinear seismic metasurface," Int. J. Mech. Sci. **221**, 107189 (2022).

[52]C. Sugino, S. Leadenham, M. Ruzzene et al., "On the mechanism of bandgap formation in locally resonant finite elastic metamaterials," J. Appl. Phys. **120**(13), 134501 (2016).

[53]Y. Xue, J. Li, Y. Wang et al., "Broadband vibration attenuation in nonlinear meta-structures with magnet coupling mechanism: Theory and experiments," Commun. Nonlinear Sci. Numer. Simul. **127**, 107543 (2023).

[54]Y. Jian, L. Tang, G. Hu et al., "Design of graded piezoelectric metamaterial beam with spatial variation of electrodes," Int. J. Mech. Sci. **218**, 107068 (2022).

[55]M. Berardengo, S. Manzoni, O. Thomas et al., "The reduction of operational amplifier electrical outputs to improve piezoelectric shunts with negative capacitance," J. Sound Vib. **506**, 116163 (2021).

[56]G. Wang, J. Cheng, J. Chen et al., "Multi-resonant piezoelectric shunting induced by digital controllers for subwavelength elastic wave attenuation in smart metamaterial," Smart Mater. Struct. **26**(2), 025031 (2017).

[57]C. Sugino, M. Ruzzene, and A. Erturk, "Design and analysis of piezoelectric metamaterial beams with synthetic impedance shunt circuits," IEEE/ASME Trans. Mechatron. **23**(5), 2144–2155 (2018).

[58]D. Xia, X. Pu, S. Tong et al., "Piezoelectric metamaterial with digitally controlled nonlinear shunt circuit for broadband wave attenuation," Appl. Phys. Lett. **124**(12), 121704 (2024).

[59]Y. Jian, G. Hu, L. Tang et al., "A generic theoretical approach for estimating bandgap bounds of metamaterial beams," J. Appl. Phys. **130**(5), 054501 (2021).

[60]B. Zhao, H. R. Thomsen, J. M. De Ponti et al., "A graded metamaterial for broadband and high-capability piezoelectric energy harvesting," Energy Convers. Manage. **269**, 116056 (2022).

03 August 2024 11:14:43